

Comparing landslide patterns and failure mechanisms in restored and native forest ecosystems: Insights from geomorphology, lithology and vegetation

Ni An ^{a,*}, Zhisheng Dai ^a, Xie Hu ^{b,*}, Buqing Wang ^{c,d}, Zhitao Huo ^{c,d}, Yuexin Xiao ^{c,d}, Wei Zhan ^e, Yongyong Yang ^e

^a College of Civil Engineering and Architecture, Zhejiang University, Hangzhou 310058, China

^b College of Urban and Environmental Sciences, Peking University, Beijing 100871, China

^c Changsha Natural Resources Comprehensive Investigation Center, China Geological Survey, Changsha 410600, China

^d Huangshan Observation and Research Station for Land-Water Resources, Huangshan 245400, China

^e Zhejiang Scientific Research Institute of Transport, Hangzhou 310058, China

ARTICLE INFO

Keywords:

Lithology-vegetation interaction
Extreme rainfall events
Group-occurring landslides
Restored and native forest ecosystems

ABSTRACT

Climate change has led to an increasing frequency of extreme rainfall events, intensifying the group-occurring landslides on a global scale. However, the role of forest management measures, particularly the combined effects of geomorphology, lithology and vegetation conditions, in controlling the occurrence and characteristics of these landslides remains poorly understood. A detailed field investigation and statistical analyses based on an event with around 1,673 landslides in southeastern China are conducted herein. The results reveal distinct failure patterns and mechanisms associated with different lithology-vegetation systems. Restored forest ecosystems, typically established on thick residual soil, predominantly experience short and wide landslides. However, native forest ecosystems, where landslides are controlled by soil-bedrock discontinuities, exhibit elongated and slender failure patterns that may evolve into debris flows under favorable conditions. This work provides new insights into the failure mechanisms of group-occurring landslides in restored and native forest ecosystems, offering region-specific insights into the development of ecosystem-specific ecological management strategies in the geo-hazard prevention with broader implications for subtropical monsoon areas.

1. Introduction

With ongoing global climate change, the frequency and intensity of extreme weather events, including typhoons, extreme rainfall, and anomalous high temperatures, have increased significantly. It has led to a rising trend in both the occurrence and scale of landslides, particularly in countries within the Global South, e.g., Brazil, China, the Philippines, and Vietnam (Haque et al., 2019; IPCC, 2022; Ozturk et al., 2022; Wood et al., 2016; An et al., 2020). Among various types of geo-hazards, rainfall-induced group-occurring landslides have become increasingly prevalent worldwide. Recent catastrophic group-occurring landslides exemplify the growing threat posed by extreme rainfall events. Between late April and early May 2024, the southernmost state of Rio Grande do Sul, Brazil, experienced the most severe extreme rainfall event on record, triggering over 15,000 landslides across 130 municipalities,

covering 63,000 km². The disaster affected over 2 million people, displacing or leaving 500,000 individuals homeless, causing 183 fatalities, and leaving 27 persons missing (Egas et al., 2024). In July 2024, Typhoon “Gaemi” triggered 19,513 landslides and 45,629 collapses in Zixing, Hunan, China. The disaster resulted in power outages in 149 villages and 1,714 households (11,869 rooms) collapsed, leading to 50 fatalities and 15 missing persons (China News Service Online, 2024). These events are characterized by shallow depths, high quantities, large spatial densities, and significant destructive potential, posing severe risks to human life, infrastructure, and ecosystems (Sassa, 2013; Bellugi et al., 2015).

Rainfall-induced group-occurring landslides predominantly develop within depositional soils or weathered layers, with sliding depths typically ranging from 0.5 to 3 m. These failures are often initiated at hydrological discontinuities within slopes, such as the interface between

* Corresponding authors.

E-mail addresses: anni@zju.edu.cn (N. An), hu.xie@pku.edu.cn (X. Hu).

soil and bedrock (Sidle & Bogaard, 2016; Forte et al., 2019; Paronuzzi & Bolla, 2023). The forest management measures, including deforestation and the expansion of economic forestry plantations, can significantly alter slope hydrology and stability (Li et al., 2022). Traditionally, it is agreed that the removal of vegetation cover reduces the mechanical reinforcement provided by plant roots, thereby weakening slope stability and increasing landslide susceptibility in mountainous regions (Depicker et al., 2021; Kim et al., 2017; Giarola et al., 2024). However, the Grain for Green project launched on China Loess Plateau in 1999, has led to a significant increase in vegetation coverage from 32 % in 1999 to 63 % in 2018, and a noticeable decrease in soil erosion (Hu & Zhang, 2020; Yu et al., 2024). Many group-occurring landslides on vegetated slopes of the Loess Plateau were still reported, e.g., in July 2013, 370 and 47,005 shallow landslides occurred in Yan'an, Shaanxi, and Tianshui, Gansu, respectively (Dai et al., 2022; Deng et al., 2022; Zhuang et al., 2024). Hence, it is necessary to investigate the impact of forest management measures on the occurrence of these landslides.

The modifications of forest management measures affect both canopy structure and root system characteristics via lithology-vegetation interactions, thereby modifying the slope infiltration dynamics, soil hydro-mechanical responses, and slope stability (Sato & Shuin, 2025). In response to climate change adaptation and mitigation, forestry management strategies have been proposed to enhance slope stability and reduce landslide risks (De Jesús Arce-Mojica et al., 2019). For example, replacing shallow-rooted spruce monocultures, mixed-leaf forests characterized by deeper root systems could effectively improve soil reinforcement and mitigate landslide occurrence probability with climate-resilient (Maraun et al., 2022). In restored forests (RF), implementing adaptive harvest and regeneration strategies that align with species-specific growth dynamics is essential to maintain belowground reinforcement and avoid root-system degradation that could elevate slope failure risk (Phillips et al., 2024; Sato & Shuin, 2025). In native forest (NF) regions particularly vulnerable to landslides, many actions, e.g., expanding protected areas, reducing deforestation pressure, and facilitating natural regeneration, are suggested to reduce the long-term landslide risk and support biodiversity conservation as well (Pohl et al., 2009; Li et al., 2022). However, to authors' knowledge, the relative importance of forest management measures in terms of restored forest (RF) and native forest (NF) ecosystems in the group-occurring landslides drivers and the underlying mechanisms are still not well understood.

To address the issues outlined above, a comprehensive field and numerical investigation on a rainfall-induced group-occurring landslide event located in Nanping, Fujian Province, in southeastern China, is conducted. The spatial distribution and geometric characteristics of these landslides are revealed. Six lithological zones are recognized and divided into two ecosystems by considering the forest management measures: RF and NF ecosystems. Statistical analysis is conducted to investigate the geomorphology, lithology and vegetation conditions, which allows further explanation into two patterns of shallow landslides and their failure mechanisms, respectively. Moreover, the development of ecosystem-specific ecological management strategies for RF and NF ecosystems is suggested for landslide mitigation.

2. Geographic and geological setting

The study area is situated in Nanping, Fujian Province, on the southeastern margin of the South China Block, along the inland flank of the Southeast Coastal active tectonic belt. The regional structural framework is dominated by NE–NNE-trending faults, and both historical and modern seismicity are characterized by scattered small events, suggesting a low risk of large earthquakes (Liu, 1997). The landscape is predominantly mountainous and hilly, with approximately 90 % of the land surface characterized by mountainous terrain. Elevation generally decreases from northwest to southeast (Fu, 2023). The region is characterized by a subtropical monsoon climate under the influence of the

western Pacific subtropical high. Rainfall is highly seasonal, with the majority occurring from April to September. During May–June, the quasi-stationary Meiyu front develops as the warm, moisture-laden southwesterly flows of the South China Sea branch of the East Asian summer monsoon converge with lingering cold air masses associated with the weakening East Asian winter monsoon, creating a persistent frontal zone conducive to prolonged rainfall. From July to September, typhoon landfalls further enhance precipitation, often delivering short-duration, extreme rainfall events that markedly increase slope instability (Sheng et al., 2023).

The studied landslide was triggered by an extreme, short-duration rainfall between 03:00 and 15:00 local time on 28 June 2021, during the “Dragon Boat Water” period between 03:00 and 15:00 on June 28, 2021. Hourly rainfall data from three meteorological stations near the landslide-affected areas were collected, and a 12-hour cumulative rainfall map was generated. Within the Wujiatang watershed, the extreme rainfall event triggered around 1,673 landslides within 12 h (Fig. 1a). The landslides near the three stations occurred sequentially between 11:00–12:00, 12:00–13:00, and 10:00–11:00, respectively. The 12-hour cumulative rainfall recorded at the three weather stations was 308 mm, 316 mm, and 258 mm, respectively. A comparison between landslide initiation times and peak rainfall periods reveals a sequential rather than simultaneous failure pattern, suggesting a delayed response of slope instability to rainfall infiltration (Fig. 1b). Furthermore, the 12-h cumulative rainfall map exhibits significant spatial variability, with maximum precipitation concentrated in the central region and decreasing towards the periphery. Notably, the area receiving the highest rainfall was a low-mountain region with relatively high elevation; however, this did not correspond to the zone with the highest landslide density. This observation suggests that group-occurring shallow landslides are not merely controlled by rainfall but are also influenced by geomorphology conditions, lithology conditions, and vegetation cover. Fig. 1c presents the aerial view of a representative landslide zone in the event.

3. Data and methods

3.1. Remote sensing interpretation and field investigation

High-resolution historical imagery (0.5 m spatial resolution) from Google Earth was acquired on 8 January 2020 (pre-event) and 11 November 2021 (post-event), respectively. Landslide boundaries were delineated through visual interpretation based on the comparison of geomorphological, land surface, and vegetation characteristics in the pre-event and post-event remote sensing imagery. In addition, comprehensive field surveys in 6 lithologic zones, which were located in 6 sites (details provide in Table S3). Extensive aerial photogrammetry and targeted ground field investigations were carried out to verify landslide features identified through remote sensing interpretation. Aerial surveys can provide high-resolution coverage of large areas, enabling the detection of subtle geomorphological indicators, while field inspections allow confirmation of land surface characteristics, vegetation disturbance, and slope conditions. The validation process is thus conducted based on the comparison of the typical landslide features and boundaries. Moreover, the Sentinel-2 L2A imagery in May 2021 with a resolution of 10 m provided by Google Earth Engine was also collected for pre-event cross-checking. The occurrence date and locations of the interpreted landslides, were further verified by analyzing historical rainfall information in the study area with integrating evidence collected during field interviews.

A 10 m resolution Digital Elevation Model (DEM) was integrated into ArcGIS geospatial analysis tools to extract topographic and geomorphological parameters as well as landslide geometric characteristics. The topographic and geomorphological parameters include slope gradient, aspect, elevation, relative elevation difference, plane and profile curvatures while landslide geometric characteristics consist of

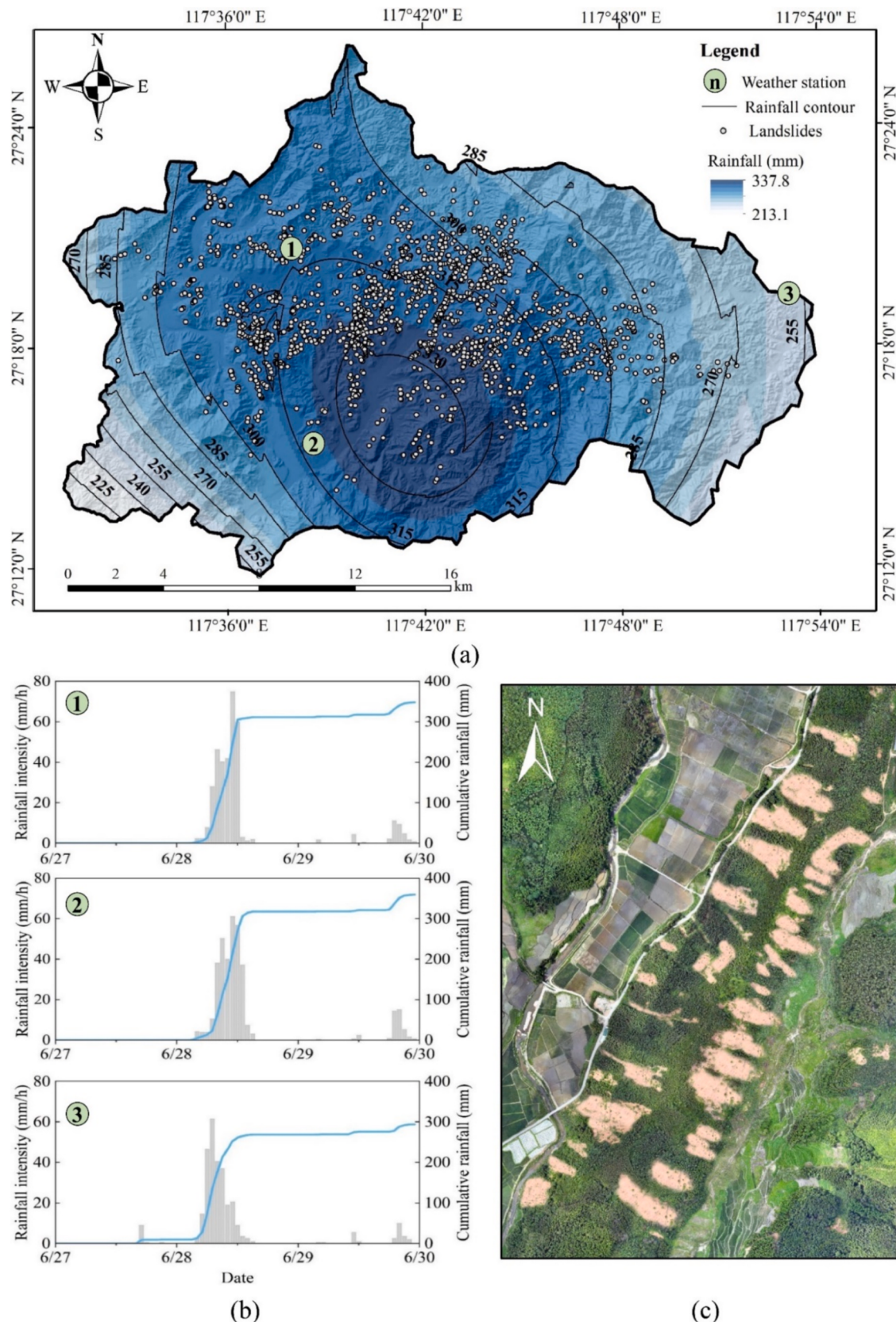


Fig. 1. Overview of the study area: (a) geographic location and 12-hour cumulative rainfall map of the extreme rainfall event with the occurred landslides recorded. (White dots indicate landslide locations, black lines denote isohyets, and triangles with numbered circles represent meteorological station. See Methods for details), (b) the variations of rainfall intensity recorded by three weather stations, and (c) aerial view of landslides occurred during the event.

area, length and width. According to the International Association for Engineering Geology (IAEG, 1990), the length is defined as the shortest distance between the highest and lowest points along the direction of landslide movement, while the width represents the maximum distance in the direction perpendicular to the length, as presented in Fig. S1-a.

To assess vegetation structure and health, multispectral UAV surveys were conducted to derive the Normalized Difference Vegetation Index (NDVI) and Normalized Difference Red Edge Index (NDRE), which characterize canopy density and photosynthetic activity, respectively (Bronson et al., 2020; Huang et al., 2020). The combination of NDVI and NDRE can offer a more robust and nuanced assessment of vegetation conditions, which allows us to better characterize the effect of vegetation on the landslide occurrence, particularly in ecosystems with dense or heterogeneous vegetation cover, e.g., RF and NF ecosystems. Since multispectral imaging cannot penetrate the canopy, a 20 m × 20 m standard plot survey was conducted in the six lithological zones to further assess the structural characteristics of vegetation, including tree species composition, planting density, tree stand age, tree height, and the tree diameter at breast height (DBH) (Fig. S1-b). The spatial distribution of root systems was analyzed using a 50 cm × 50 cm root profile window with a 10 cm × 10 cm grid (Fig. S1-c). Root diameters within the profile window were measured using a vernier caliper and categorized into four size classes: 0–1 mm, 1–2 mm, 2–5 mm, and 5–10 mm. The Root Area Ratio (RAR) was calculated across different soil depths to quantify root reinforcement effects.

$$RAR = \frac{A_r}{A} = \frac{\sum_{i=1}^n \pi d_i^2}{A} \quad (1)$$

where A_r and A represent the area of root zone and the surveyed zone (mm^2), d_i is the diameter of the i^{th} root (mm), and n is the total number of roots.

3.2. In-situ tests and laboratory experiments

To quantify in-situ infiltration rates, a double-ring infiltrometer with an outer diameter of 40 cm and an inner diameter of 20 cm was employed. After removing surface litter, the rings were inserted 5 cm into the soil. A constant water head of 10 cm was maintained, keeping equal water levels in both rings to minimize lateral flow effects. Infiltration rates were computed based on the volume of water infiltrated within the inner ring at successive time intervals. The test continued until steady-state infiltration was achieved, which was reflected by consistent infiltration rates over consecutive measurements (Wang et al., 2022).

To characterize soil stratigraphy and mechanical properties, soil profiles were excavated to the depth of the sliding surface. Based on textural/structural contrasts and hydromechanical considerations (IPCC, 2006; IUSS Working Group WRB, 2022), soils were grouped into fixed depth intervals that approximate three functional horizons: L1 (0–30 cm, macropore-rich topsoil), L2 (30–60 cm, transitional subsoil), and L3 (60–100 cm, lower residual-soil mantle near the saprolite/Cr interface). In the Ss lithologic zone with a thinner regolith (typically < 60 cm), and thus only two layers (L1, L2) were defined. This discretization ensures consistent sampling, testing, and parameterization across sites. Undisturbed soil samples in each layer were collected using ring cutters for the measurement of bulk density and direct shear tests. Additionally, 1 kg of disturbed soil samples were collected for particle size analysis and other purposes. Bulk density was measured by oven-drying method. Saturated consolidated drained direct shear tests were conducted with a shear rate of 0.02 mm/min under normal stresses of 50, 100, 150, and 200 kPa to determine effective cohesion and effective internal friction angle (ASTM International, 2023). In terms of soil particle size distribution, particles larger than 2 mm were separated using sieve analysis. Laser diffraction analysis (Malvern MS 3000) was used to quantify particle size fractions smaller than 2 mm. According to the USDA classification system,

particle size fractions were categorized as gravel (>2 mm), sand (0.05–2 mm), silt (0.002–0.05 mm), and clay (<0.002 mm).

Vegetation roots from both restored and natural forest were collected for mechanical testing. Prior to testing, the collected roots were immersed in a 5 % ethanol solution for 24 h to restore mechanical properties. Tensile tests were conducted using a universal testing machine (0–10 kN capacity, 8–10 cm gauge length) at a constant loading rate of 10 mm/min until failure (Fig. S1-d). The maximum tensile strength was estimated by:

$$T_{\max} = 4F_{\max}/\pi d_i^2 \quad (2)$$

where, T_{\max} (MPa) and F_{\max} (N) represent the maximum tensile strength and force.

3.3. Vegetated-slope stability analysis

To quantify the mechanical reinforcement effect of roots, the Wu model was employed herein (Wu et al., 1979). The Wu model assumes that all roots fail simultaneously upon slope failure, which may lead to an overestimation of root-induced cohesion. Following Preti (2006), we adopted an empirical progressive-failure factor ($k'' = 0.4$) to downscale the Wu model's assumption of simultaneous root mobilization and to account for partial tensile mobilization due to pullout/sliding and spatial heterogeneity (typical range 0.3–0.5; Preti, 2006; Vergani et al., 2017). The modified equation is expressed by:

$$c_r = k'' k' \sum_{i=1}^n 1000 \cdot T_{ri} \frac{A_{ri}}{A} \quad (3)$$

Where c_r is the root-induced cohesion (kPa), k' (set to 1.2) is an orientation/section-change factor that converts RAR measured on vertical pits to the inclined shear surface and accounts for the average inclination of roots relative to the failure surface, and T_{ri} is the average tensile strength of roots within each diameter class (MPa). This modification allows a more realistic estimation of root reinforcement by accounting for progressive root failure, rather than assuming simultaneous rupture of all roots.

In slope stability analysis, the limit equilibrium method is employed with considering the slope geometric configuration. The shear resistance (S_{sr}) is provided by the lateral and basal shear strength of the sliding mass, while the driving force (τ) is induced by the gravitational weight of the slope (Schmidt et al., 2001; Guo & Ma, 2023). The factor of safety (F_s) is estimated by:

$$F_s = \frac{S_{sr}}{\tau} = \frac{c_l A_l + c_b A_b + A_b (\rho_s - \rho_w M) g z \cos^2 \theta \tan \varphi'}{A_b (\rho_s + \rho_w M n) g z \sin \theta \cos \theta} \quad (4)$$

where A_l (m^2) is the lateral area, c_l (kPa) is the total cohesion provided by soil (c_s) and roots (c_r), A_b (m^2) is the basal area of the landslide, c_b (kPa) is the basal cohesion, ρ_s (g/cm^3) is the soil bulk density, ρ_w (g/cm^3) is the water density, M is the degree of soil saturation, n is the soil porosity, z (m) is the soil depth, θ ($^\circ$) is the slope angle, and φ' ($^\circ$) is the effective internal friction angle.

3.4. PCA analysis of landslide morphology influencing factors

The landslide area (Area) and length-to-width ratio (L/W) are important morphology indicators in the identification and risk assessment of landslides (Tian et al., 2017; Rana et al., 2021). In this study, Pearson correlation analysis is initially conducted to identify the top 10 factors most strongly correlated with landslide area and L/W. These factors are then standardized to ensure comparability across variables, eliminating any potential bias arising from differences in units of measurement. Principal component analysis (PCA) is conducted herein to quantify the contribution of geomorphology, lithology and vegetation influencing factors on the values of area and L/W of landslides

(Hartmann & Blume, 2024; Staley et al., 2023). In this method, the eigenvalues represent the amount of variance explained by each principal component (PC) and the eigenvectors define their directions in the original feature space. The loading scores describe how much each variable contributes to PC. To further investigate the similarities between samples, K-means clustering is performed on the PCA results, which led to the identification of distinct clusters. This analysis enables the identification of key geomorphological, lithological, and vegetation factors influencing landslide area and L/W.

4. Results

4.1. Spatial distribution and geometric characteristics of landslides

This study conducted a detailed field investigations and statistical analyses to examine the spatial distribution, topographic features, and geomorphological characteristics of the group-occurring landslides event in Nanping, Fujian occurred on June 28, 2021. The identified 1,673 landslides are primarily distributed across six distinct lithological zones: Granulite (Grt), Granite (Gr), Conglomerate (Cg), Quartz schist (Qs), Tuff (Tf), and Sandstone (Ss), as detailed in Fig. 2. Statistical analysis indicates that the Gr zone has the highest number of landslides (600 events) with a maximum density value of 42.62 (Table 1). Although the Cg zone has 143 landslides, its maximum landslide density is the highest (46.42) in the studied zone. Tf and Ss zones have the lowest landslide occurrences and densities, with 55 events (19.77 landslides/km²) and 124 events (22.75 landslides/km²), respectively.

In order to reflect the movement patterns, and triggering mechanisms of landslides in different lithology zones, as well as the potential influencing areas of these landslide hazards, the area and the length-to-width ratio (L/W) of the identified landslides are employed herein as key indicators to describe the landslide geometry and classification (Taylor et al., 2018; Rana et al., 2021; McCall & Cook, 2024). These landslides are mainly small and medium sizes and their areas are concentrated in the value range of 200–3000 m² (Fig. 3a). Among the six lithological

zones, the mean landslide area (μ) in the Tf and Ss zones are 1520 m² and 1372 m², respectively, larger than others. The mean landslide area in Cg zone exhibited the smallest value of 948 m².

Analysis of L/W for the occurred landslides reveals that the events in Tf and Ss zones exhibit higher values, with average values (μ) approaching 7.17 and 9.45 respectively, and larger variability (σ) compared to those in other zones (Fig. 3b). It indicates that slender landslide forms dominate in the zones of Tf and Ss, whilst the short-wide pattern are common in the zones of Grt, Gr, Cg and Qs, respectively. A high length-to-width ratio indicates an elongated and narrow morphology of landslide, suggesting a pronounced downslope movement tendency and the potential formation of debris flow when enough source of sediments and topographic condition exist. In contrast, a low length-to-width ratio corresponds to a shorter and wider shape of landslide, characterized by lateral spread and stabilization over shorter distances. However, the latter landslide pattern may cause rapid and localized damage compared to the former type (Leshchinsky et al., 2019; Qiu et al., 2024).

Based on field observations of these six lithological zones, they are classified into two types of ecosystems: RF in the Grt, Gr, Cg and Qs zones and NF in Tf and Ss zones, with consideration of the forest management measures for the following comparative analysis.

4.2. Geomorphology conditions

In order to understand the geomorphological factors influencing the initiation of these landslides in different lithological zones, six characteristics (slope gradient, aspect, elevation, relative elevation difference, plane and profile curvatures) are investigated herein (Dai et al., 2002). These landslides characteristics in six lithology zones are presented in Fig. 4 and the detailed statistical values are provided in Table S1. As the primary gravitational driving factor for landslide development, the concentration range and distribution patterns of slope gradients vary significantly across different lithological zones (Fig. 4a). Specifically, the concentrated slope ranges (normal distribution $\mu \pm \sigma$) for Grt, Ss, and Tf

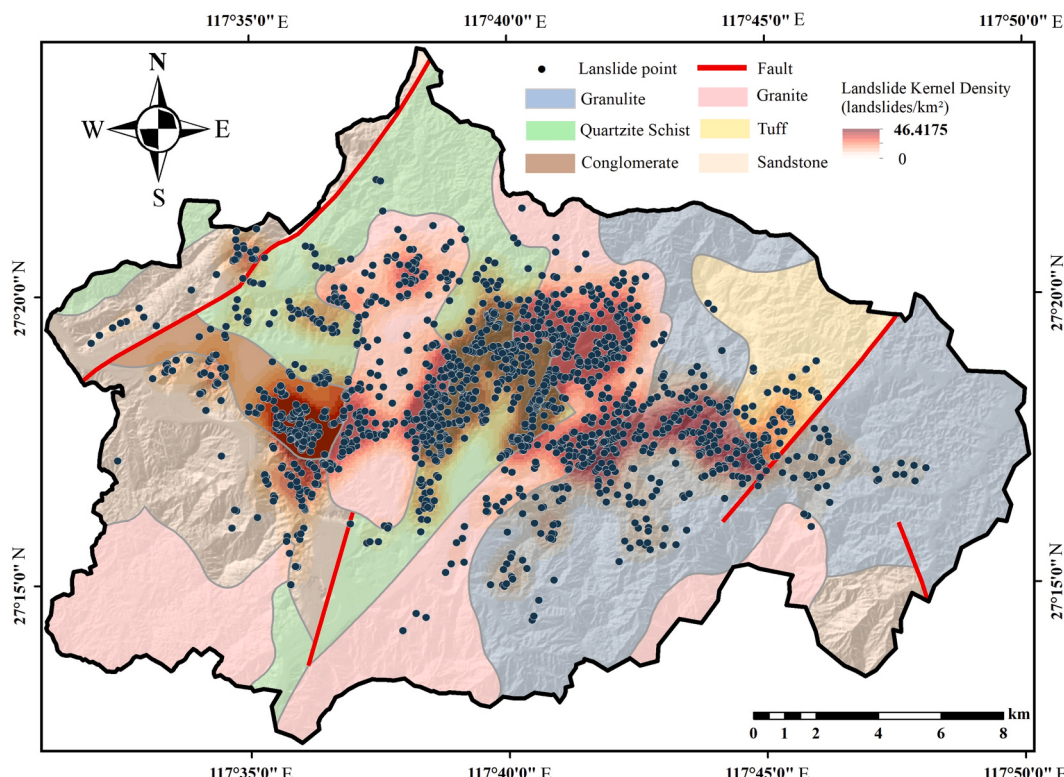
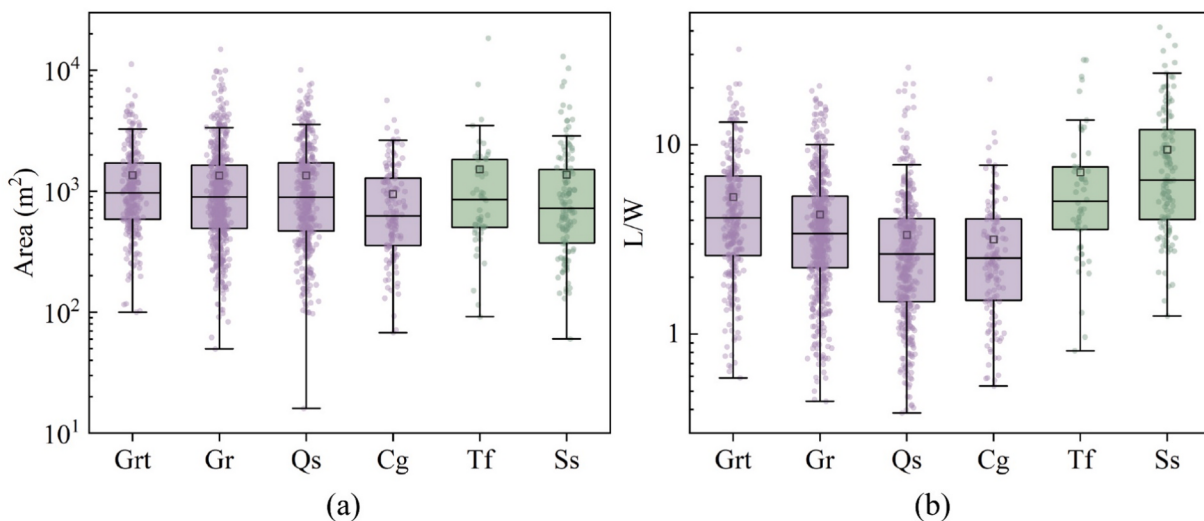


Fig. 2. Spatial distribution of landslides across six lithological zones with the statistics of landslide quantity and maximum density.

Table 1

Vegetation plot survey and tensile strength of roots across different diameter classes.

| Lithology | Ecosystem type | NDVI ($\mu + \sigma$) | NDRE ($\mu + \sigma$) | Plant density (/hm ⁻²) | Stand age (a) | DBH (cm) ($\mu + \sigma$) | Height (m) ($\mu + \sigma$) | | | | |
|--|----------------|--|-------------------------|------------------------------------|---------------|-----------------------------|-------------------------------|--|--|--|--|
| Grt | RF | 0.82 ± 0.03 | 0.32 ± 0.05 | 2975 | 23 | 13.5 ± 4.3 | 10.7 ± 3.0 | | | | |
| Gr | RF | 0.85 ± 0.03 | 0.37 ± 0.08 | 1675 | 32 | 16.7 ± 6.4 | 11.7 ± 2.2 | | | | |
| Cg | RF | 0.79 ± 0.05 | 0.29 ± 0.06 | 3175 | 22 | 12.1 ± 2.5 | 11.2 ± 2.5 | | | | |
| Qs | RF | 0.82 ± 0.07 | 0.33 ± 0.06 | 4850 | 20 | 11.4 ± 8.8 | 9.3 ± 2.8 | | | | |
| Tf | NF | 0.82 ± 0.04 | 0.32 ± 0.05 | 1625 | 34 | 8.3 ± 5.3 | 8.8 ± 4.0 | | | | |
| Ss | NF | 0.55 ± 0.12 | 0.21 ± 0.06 | 1450 | 36 | 6.3 ± 4.9 | 8.7 ± 4.9 | | | | |
| Tree species | | Average tensile strength of root (MPa) | | | | | | | | | |
| | | 0–1 mm | | 1–2 mm | | 2–5 mm | | | | | |
| <i>Cunninghamia lanceolata</i> (Lamb.) Hook. | | 26.01 | | 20.71 | | 13.81 | | | | | |
| <i>Pinus massoniana</i> Lamb. | | 24.14 | | 23.37 | | 13.29 | | | | | |
| | | 5–10 mm | | | | | | | | | |
| | | 4.88 | | | | | | | | | |
| | | 3.71 | | | | | | | | | |

**Fig. 3.** Geometric characteristics of landslides in six lithology zones: (a) area and (b) length-to-width ratio.

are 19.5°–32.5°, 19.3°–34.0°, and 21.9°–31.59°, respectively, indicating a higher susceptibility to landslides in relatively steep mid-slope areas within these zones (Table S1). The concentrated slope ranges for Gr, Cg, and Qs are 16.9°–31.7°, 10.0°–25.0°, and 14.7°–30.2°, respectively, which reflects the prone of landslide occurrence in low to moderate slope areas. The landslides events mainly occurred in the south-facing slope in Grt, Gr, Tf and Qs zones, whilst in south-east-facing slopes in Cg and Ss zones (Fig. 4b). It reveals the “sunlight” inclination of the occurred landslides, which may be attributed to the differences of slope hydro-thermal response in south-facing and north-facing slopes under the same meteorological conditions. Fig. 4c presents the concentration of slope elevations of 200–500 m in the occurred landslides, while a smaller proportion occurred in low-mountain areas at elevations of 500–1000 m. Further comparisons in terms of the elevation differences (Fig. 4d) indicate that the landslides in Tf and Ss zones exhibit the largest elevation differences, whereas those in Cg zones had the lowest elevation differences.

Plan curvature governs the convergence (negative) or divergence (positive) of materials or water along the direction of landslide movement (Ohlmacher, 2007). As shown in Fig. 4e, landslides in Grt, Gr, Tf, and Ss are predominantly developed in convergent terrains with negative plan curvature. In contrast, landslides in Cg and Qs zones are distributed in both convergent and divergent areas. Profile curvature influences the distribution of driving and resisting stresses along the direction of landslide movement (Montgomery & Dietrich, 1994). As shown in Fig. 4f, landslides in Tf and Ss zones predominantly develop in convex slope areas dominated by tensile stresses. However, landslides in Grt, Gr, Qs, Cg zones are distributed across both concave and convex

slope regions, experiencing both compressive and tensile stresses.

4.3. Lithology condition and soil properties

Fig. 5 present the excavated soil profiles (Ss with two layers: L1 (0–30 cm) and L2 (30–60 cm); others with three layers: L1 (0–30 cm), L2 (30–60 cm), and L3 (60–100 cm)) and particle size distribution at different depths near the landslide initiation locations in six lithological zones. Specifically, for those landslides occurred in RF ecosystems, their sliding surfaces develop within residual soil, typically at a depth of ~ 1 m. However, in terms the NF ecosystems, the sliding surfaces of landslides occur at the interface between the weathered layer and bedrock, at depths of 0.6 m for Tf zones, and 1 m for Ss zones, respectively.

The residual soil profiles in RF ecosystems (Grt, Gr, Cg and Qs) exhibit distinct stratification, with silt as the dominant component across all layers. The soil profile of Grt shows well-defined layering, with L1 (0–30 cm) being light brown and loosely structured, L2 (30–60 cm) darker and more compact, and L3 (60–100 cm) reddish-brown with partially weathered parent rock fragments. Similar characteristics can be observed in Gr. The soil of Cg was uniformly light reddish-brown containing small, well-rounded gravel particles with high SiO₂ content in all layers. However, soil profile in Qs presents brick-red color and clay-rich texture, with quartz particles and small rock fragments in L3, which indicates an intense oxidation and weathering process. In Grt and Qs, sand and gravel content increased gradually, while silt and clay content declined as depth increases. While the proportions of sand, gravel, and clay fluctuated slightly with depth in Gr and Cg.

The soil profiles in NF ecosystems (Tf and Ss) exhibit higher gravel

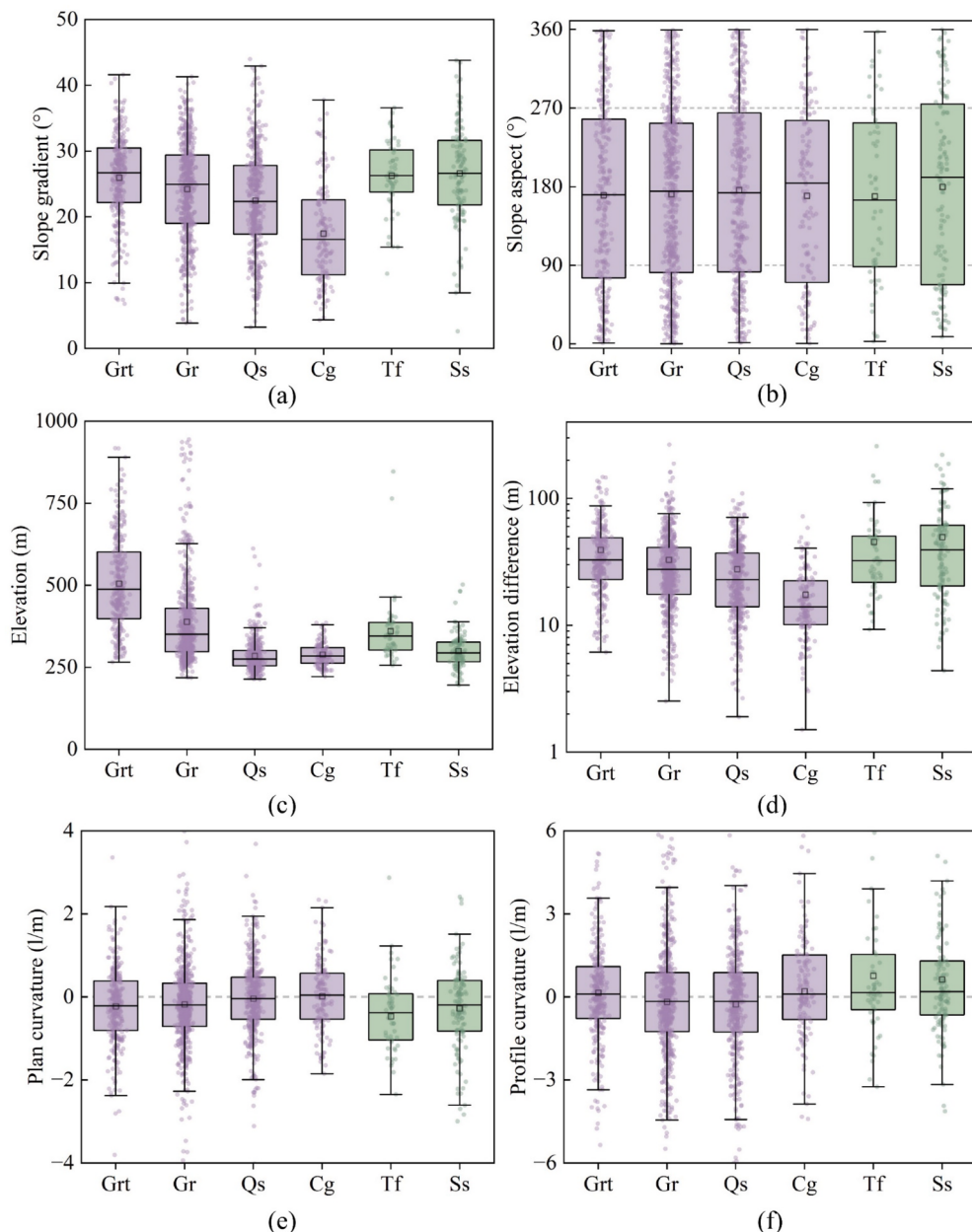


Fig. 4. Landslide characteristics in six lithology zones: (a) slope gradient, (b) aspect distribution, (c) elevation distribution, (d) elevation difference, (e) plan curvature, and (f) profile curvature.

and sand content, promoting increased permeability and deeper infiltration pathways. In Tf, soil was predominantly light yellow–brown and composed of irregularly shaped gravel and silt. Bedrock exposure can be observed at the bottom of L3. While the soil profile of Ss was light yellow–brown with a loose structure. The L2 layer containing fresh sandstone gravel were based on sandstone bedrock. Moreover, in Tf, gravel content increased with depth (43 %, 49 %, and 68 % in L1, L2, and L3, respectively), whereas silt content decreased from 36 % in L1 to 20 % in L3. In Ss, the gravel and sand fraction increased from 23 % (L1) to 55 % (L2). The contents of gravel and sand in both Tf and Ss go up significantly as the depth increases, indicating the higher permeability in L2 and L3, respectively. Across all lithological zones, sand and gravel content increase more or less, while clay content keeps a decreases tendency due to progressive weathering processes.

The bulk density (Fig. 6a), infiltration rate (Fig. 6b), cohesion (Fig. 6c) and internal friction angle (Fig. 6d) characterize the hydro-mechanical properties of the soils across different lithological zones.

The results indicate distinct mechanical behaviors between RF (Grt, Gr, Cg and Qs) and NF ecosystems (Tf and Ss). Soils in NF ecosystem exhibit higher bulk density than those in RF ecosystem. Across all lithological zones, bulk density increases with depth (Fig. 5a), corresponding to higher compaction and reduced porosity in deeper soil layers. The infiltration rates in NF ecosystems are higher than those in RF ecosystems, which are consistent with the particle size distribution as presented in Fig. 5b.

As shown in Fig. 6c, in NF ecosystems, soil cohesion values at the sliding surface are 2.89 kPa (L3, Tf) and 1.29 kPa (L2, Ss), respectively. In RF ecosystems, soil cohesion values near the sliding surface are 5.18 kPa (L3, Grt), 5.71 kPa (L3, Gr), 6.29 kPa (L3, Cg), and 7.05 kPa (L3, Qs), respectively. Hence, soils in NF ecosystems exhibit significantly lower values than those in RF ecosystems, suggesting weaker interparticle bonding and higher susceptibility to shear failure. The lowest cohesion values are consistently observed near the sliding surface in all lithological zones. Moreover, soils in NF ecosystems own higher values of

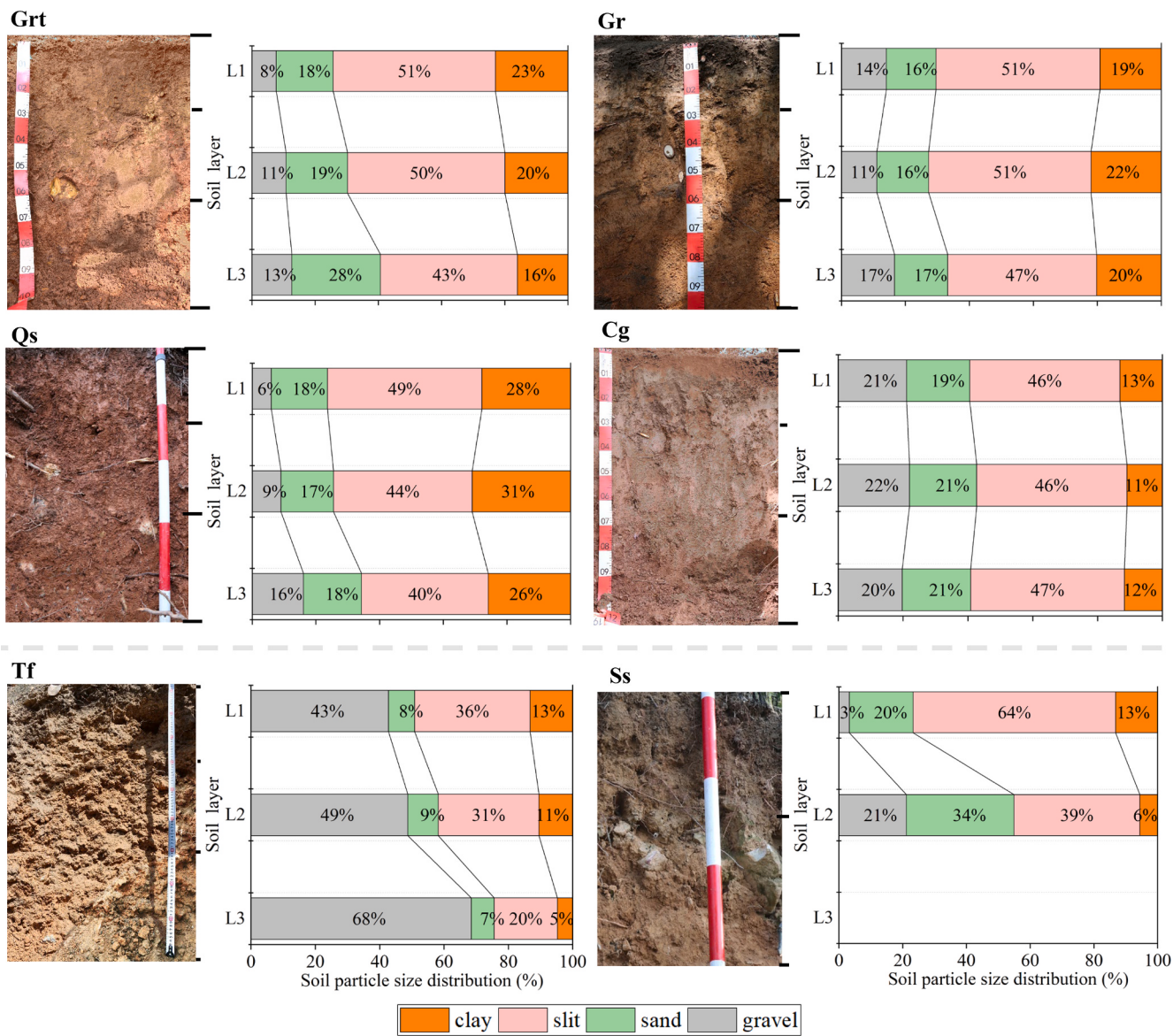


Fig. 5. The excavated soil profiles in six lithological zones, and the corresponding particle size distribution for different layers.

friction angle compared to those in RF ecosystems, indicating greater resistance to shear displacement despite lower cohesion (Fig. 6d). The maximum friction angle in most lithological zones appears near the sliding surface except the case of Qs. Overall, soils at the sliding surface depth of all six lithological zones exhibit lower cohesion but higher friction angles compared to other depths, which may be attributed to the higher content of coarse particles at these depths.

4.4. Vegetation structure and root system distribution

The Normalized Difference Vegetation Index (NDVI), Normalized Difference Red Edge Index (NDRE), and vegetation structural characteristics, including tree species composition and forest stand parameters, are detailed in Table 1. In RF ecosystems and the Tf zone in NF ecosystems, NDVI values range from 0.8 to 0.85, indicating a dense canopy cover. However, NDVI in the Ss zone of NF is significantly low with an average value of 0.55 and high variability of 0.12. It may be related to the shallow and nutrient-deficient soil layer, which constrains the aboveground biomass accumulation. NDRE values exhibit a similar variation trend to NDVI, suggesting a positive correlation between canopy density, photosynthetic efficiency, and overall vegetation

health.

The RF ecosystems are dominated by *Cunninghamia lanceolata* (Lamb.) Hook. Specifically, the Gr zone exhibits the highest value of stand age, DBH, and tree height, but has the lowest planting density among all zones. The vegetation structural characteristics in Grt and Cg zones are similar. However, the Qs zone presents the highest planting density, lower values of stand age, DBH, and height with relatively high structural variability, compared to other zones in RF ecosystems. The collected vegetation condition reflects the potential inefficiencies in silvicultural strategies. In NF ecosystems (Tf and Ss), soils are shallow with high gravel content, resulting in low water retention capacity. Due to minimal human intervention, these zones are characterized by NF dominated by *Pinus massoniana* Lamb., *Schima superba* Gardn. et Champ., *Cyclobalanopsis championii* (Bentham) Oersted, and *Liquidambar formosana* Hance. NF exhibits higher stand age but substantially lower planting density, DBH, and tree height compared to RF in Group (1). Among all six lithological zones, the Ss zone has the lowest values of planting density, DBH, and tree height, revealing the limited productivity and growth potential of vegetation in this region due to poor soil conditions.

The root system profile survey reveals that plant roots in all six

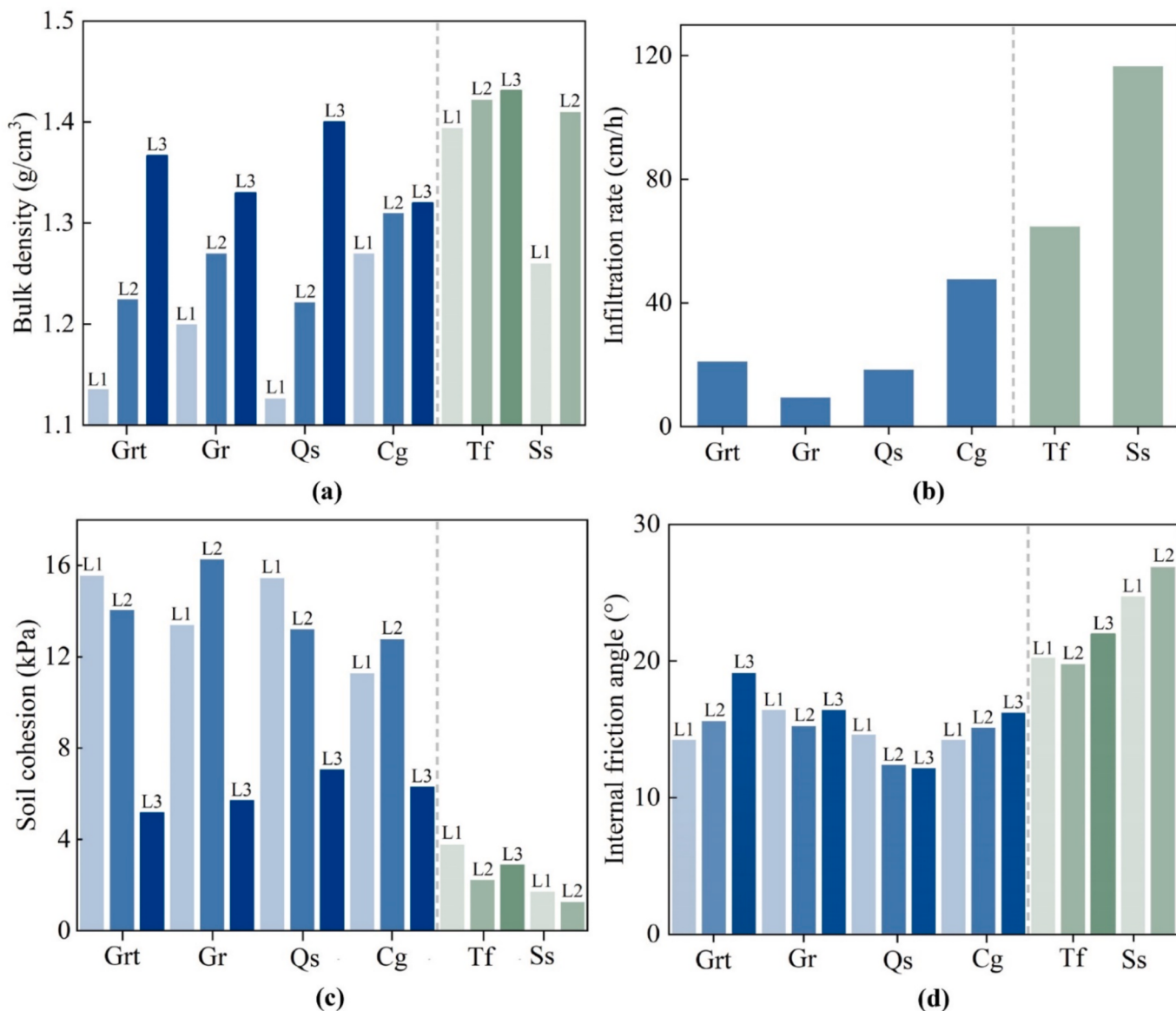


Fig. 6. The measured values of soil (a) bulk density, (b) infiltration rate, (c) soil cohesion and (d) internal friction angle at different depths in six lithological zones.

lithological zones are primarily distributed in the depths of 40–60 cm, entirely above the sliding surface (Fig. 7). Consequently, root systems do not directly contribute to the slope stability. In RF ecosystems, despite the uniform plantation of *Cunninghamia lanceolata* (Lamb.) Hook., the cumulative values of root area ratio (RAR) at the studied profiles follow the order: Grt > Cg > Gr > Qs and the total root quantity are ranked as: Cg > Gr > Grt > Qs. NF ecosystems are dominated by *Pinus massoniana*, which exhibits significantly lower RAR and root quantity across soil layers compared to those in RF ecosystems. These findings suggest that root distribution is influenced by both species-specific genetic factors and soil properties in various lithological conditions (Sakals & Sidle, 2004; Stokes et al., 2009).

Moreover, the measured root tensile strength values for *Cunninghamia lanceolata* (Lamb.) Hook. (RF) and *Pinus massoniana* (NF) across different diameter classes are detailed in Table 1. Generally, root tensile strength decreases as root diameter increases. For diameter classes of 0–1 mm, 2–5 mm, and 5–10 mm, *Cunninghamia lanceolata* (Lamb.) Hook. exhibits slightly higher tensile strength than *Pinus massoniana*. However, in the 1–2 mm diameter class, the opposite result is observed. The root-induced cohesion values, derived by integrating RAR and root tensile strength across diameter classes (see Methods), are presented in Fig. 7.

Root-induced cohesion and RAR gradually decrease with depth in all six lithological zones. The mean root-induced cohesion in RF ecosystems is significantly higher than in NF ecosystems, revealing the reinforcement role of plantation species in enhancing shallow soil stability.

5. Discussion

5.1. Insights into the landslide patterns in RF and NF ecosystems

Field investigations of geomorphology, lithology and vegetation conditions indicate that vegetation characteristics are strongly influenced by slope topography, geomorphic attributes, and soil properties, which collectively drive different land-use patterns across the six lithological zones. The lithological zones in RF ecosystems are characterized by gentle topography, high fine particle content (clay and silt), enhanced soil fertility, and satisfactory water retention capacity within a relatively thick residual soil layer (>5 m). These favorable conditions for vegetation growing are reflected in elevated values of NDVI, NDRE, plant density, DBH, and vegetation height in the Grt, Gr, Cg, and Qs zones, as detailed in Table 1. Consequently, these lithological zones were subject to intensive anthropogenic activity, including the large-

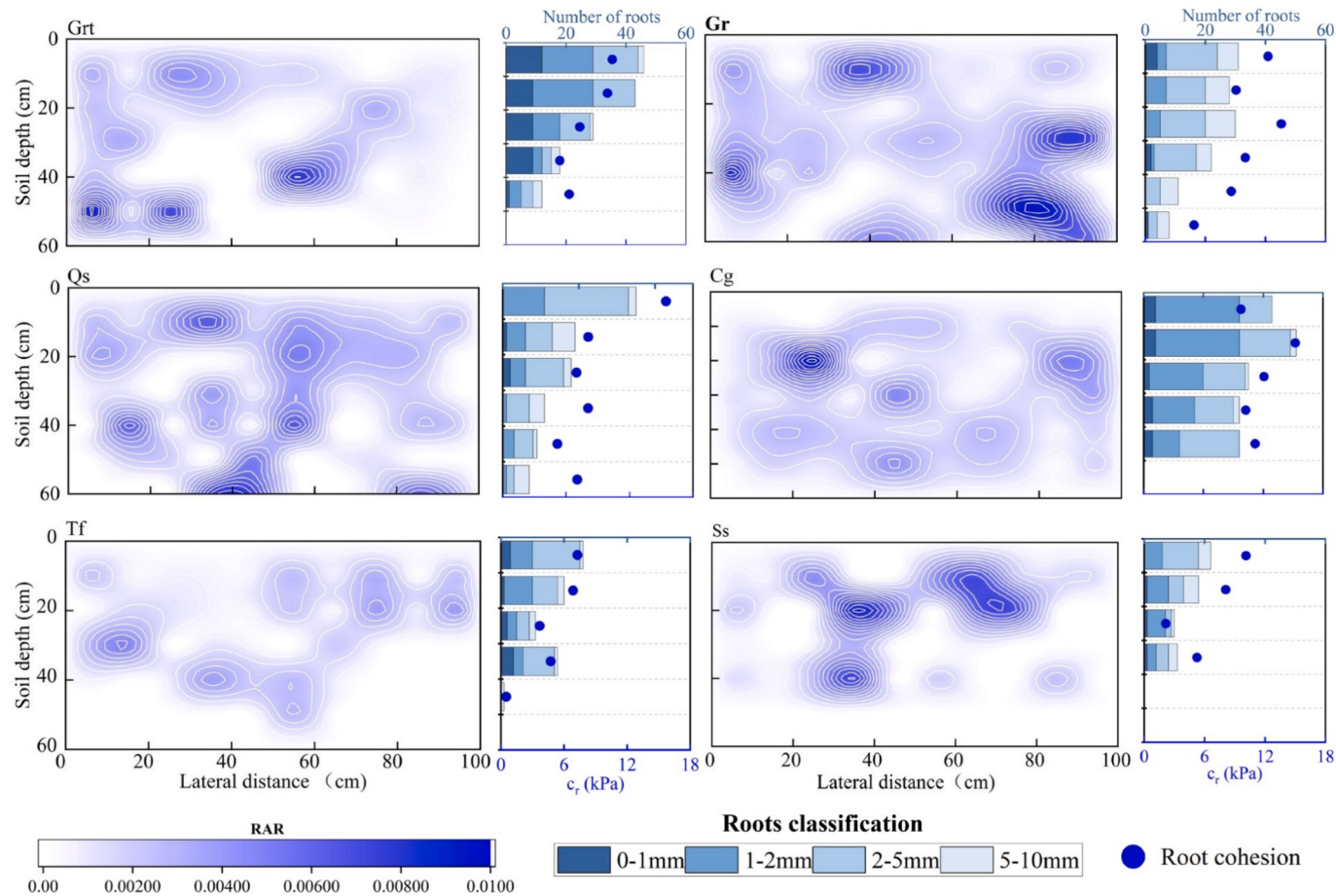


Fig. 7. Variations in root RAR, root quantity, and root-induced cohesion with depth: (The contour map represents the RAR distribution of tree roots parallel to the landslide movement direction. The bar chart illustrates the distribution of root quantity across different soil depths for the 0–1 mm, 1–2 mm, 2–5 mm, and 5–10 mm root diameter classes. Blue scatter points indicate root-induced cohesion at different soil depths.). (For interpretation of the references to color in this figure legend, the reader is referred to the web version of this article.)

scale cultivation of commercial tree species, such as *Cunninghamia lanceolata* (Lamb.) Hook., and gradually evolved into the RF ecosystems.

In contrast, the Tf and Ss zones of NF ecosystems exhibit large elevation differences, steep slopes, and convergent terrains with negative plan curvature prone to hydraulic erosion, alongside a high proportion of coarse particles (gravel and sand) and low water retention capacity due to a thin soil layer (<1 m) overlying bedrock. These factors impose significant constraints on land development and agricultural expansion, leading to the persistence of NF ecosystems in these areas.

The area and L/W of landslides are important indicators in the identification and risk assessment of landslides (Tian et al., 2017; Rana et al., 2021). Principal component analysis (PCA) is conducted herein to quantify the contribution of geomorphology, lithology and vegetation influencing factors on the values of area and L/W of landslides, as presented in Fig. 8. (Hartmann & Blume, 2024; Staley et al., 2023). In this method, the eigenvalues represent the amount of variance explained by each principal component (PC) and the eigenvectors define their directions in the original feature space. The loading scores describe how much each variable contributes to PC. The sum of PC1 and PC2 account for 84.9 % and 88.0 % of variance in terms of landslide area and L/W. Hence, they are retained to represent the characteristics of all influencing factors for further analysis.

Based on Pearson Correlation, the top 10 influencing factors related to the values of landslide area include geomorphology indicators (slope gradient, elevation difference, plan curvature, and L/W), lithology indicators (soil friction angle, silt content, soil and root cohesion) and vegetation indicators (root number, and tree height). In Fig. 8a, the

results of PCA show that PC1 is characterized by positive loading scores of slope gradient, elevation difference, L/W and soil friction angle, and negative loading scores of other factors. It indicates that slopes with larger gradient, higher values of elevation difference and soil friction angle prone to develop landslide with larger area. Moreover, landslide L/W and area present a positive correlation, which indicates that larger landslide tends to be exhibited with an elongated shape. In contrast, soils with high values of friction angle, silt content, and cohesion, and vegetations with high values of root cohesion, root number, and tree height can restrict the development of landslide area. Moreover, the loading scores of root number and soil cohesion in PC2 are positive but extremely low, which reflects the slight contribution of them to the landslide area. In conclusion, the geomorphology and lithology factors, e.g., slope gradient, elevation difference, L/W and soil friction angle, dominates the scale of landslide areas, while the lithology and vegetation factors, e.g., silt content, tree height, soil and root cohesion, inhibiting the escalation of landslide area.

In terms of the values of L/W, the top 10 influencing factors, i.e., geomorphology indicators (slope gradient, elevation difference, profile and plane curvature), lithology indicators (soil friction angle, infiltration rate, soil cohesion) and vegetation indicators (NDVI, root number, and DBH), are selected via Pearson Correlation. As presented in Fig. 8b, PC1 is dominated by positive loadings from elevation difference, slope gradient, soil friction angle, profile curvature and infiltration rate. These results indicate that slope with larger values of elevation difference, slope gradient, soil friction angle, profile curvature and infiltration rate facilitate the formation of landslide with higher L/W (Milledge et al.,

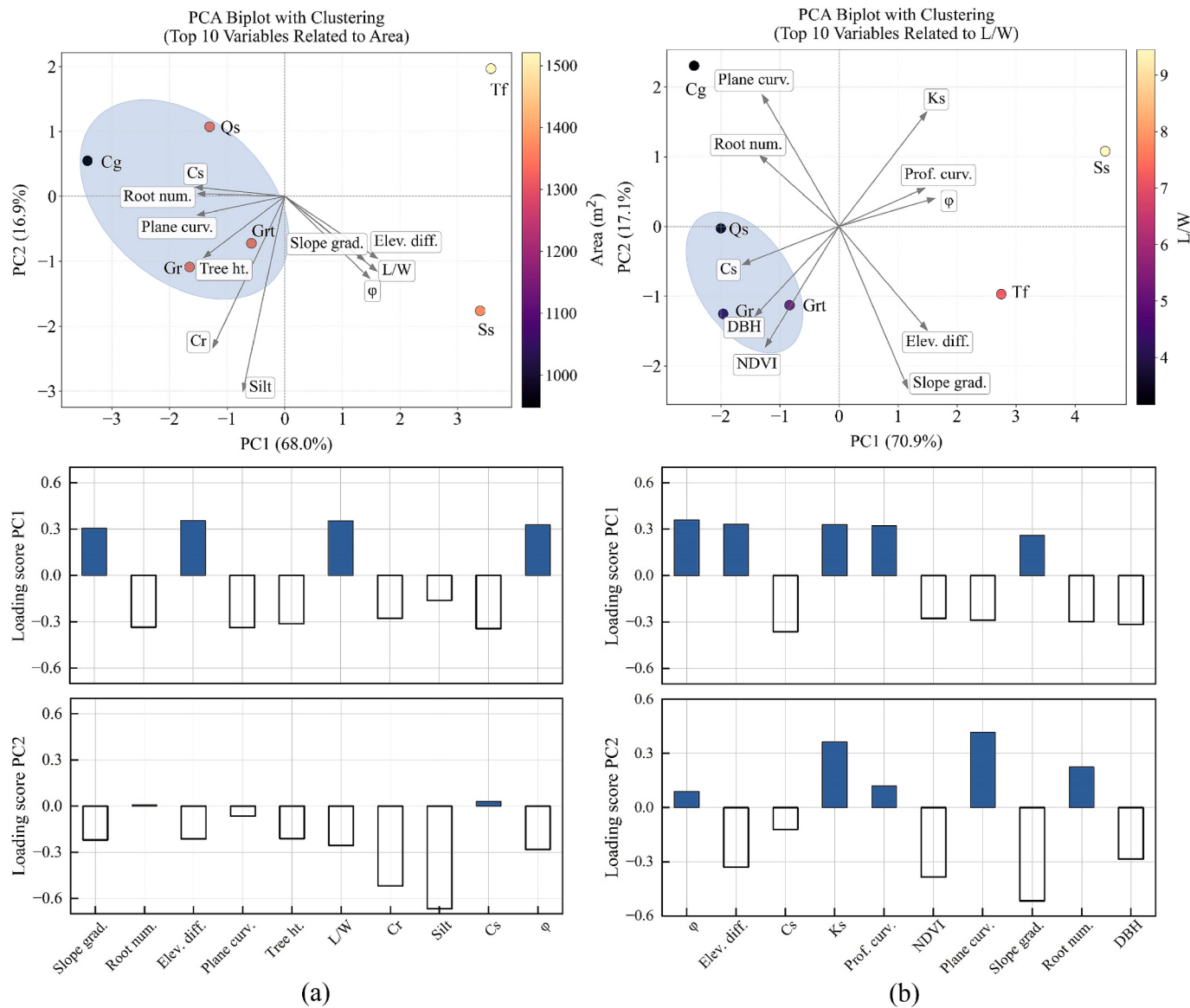


Fig. 8. PCA analysis of the contributions of multi-influencing factors to the values of landslide area and L/W (root cohesion- c_r , soil cohesion- c_s , internal friction angle- φ , infiltration rate- K_s).

2014). In contrast, other factors, e.g., plane curvature, NDVI, root number, soil cohesion, contribute negatively to PC1, suggesting that slope with negative plane curvature, dense vegetation coverage with well-developed root systems and high soil cohesion are prone to generate landslide with shorter and wider shape. In addition, the high positive loading scores of plane curvature and root number in PC2 indicate their secondary roles to the formation of elongated landslide. In summary, geomorphology and lithology indicators, e.g., elevation difference, slope gradient, profile curvature, and infiltration rate, are the primary drivers of landslide elongated shape, while soil-vegetation conditions, e.g., DBH, NDVI, and soil cohesion can restrain the spatial expansion of landslide.

In addition, the PCA analysis highlights how lithologic domains are differentiated in principal component space according to key controlling factors. Tf and Ss are positioned on the positive side of PC1, associated with other positive loadings of slope, e.g., slope gradient, elevation difference, and friction angle (φ), suggesting that steeper slopes with pronounced elevation difference and higher basal shear strength tend to produce landslides of larger area and higher L/W. In contrast, Grt, Gr, Qs, and Cg cluster on the negative side of PC1, near plane curvature, root

number, and soil cohesion (C_s), etc., indicating that areas with convergent terrain, denser vegetation, stronger root reinforcement, and higher soil cohesion contribute to landslide with smaller areas and lower L/W. This pattern underscores the coupled influence of geomorphology, lithology, and vegetation in shaping both the scale and geometric morphology of landslides. Based on the above-mentioned statistical and PCA analysis, two distinct landslide patterns can be summarized within RF and NF ecosystems, as presented in Fig. 9a and 9b, respectively.

- Pattern 1: In RF located in the Grt, Gr, Cg, and Qs zones, landslides predominantly occur on southeast-facing slopes, exhibiting lower slope gradient, smaller relative elevation differences, smaller area and lower L/W, supported by Fig. 8a. These landslides display a mix of positive and negative values of plane and profile curvatures, indicating a diverse range of slope geometries. Moreover, their morphological features are predominantly short and wide (Fig. 8b and 9a), typically inducing localized and rapid surface disruptions with limited potential for triggering secondary hazards.
- Pattern 2: In NF located in the Tf and Ss zones, where landslide quantity and density are lower, failures are primarily concentrated

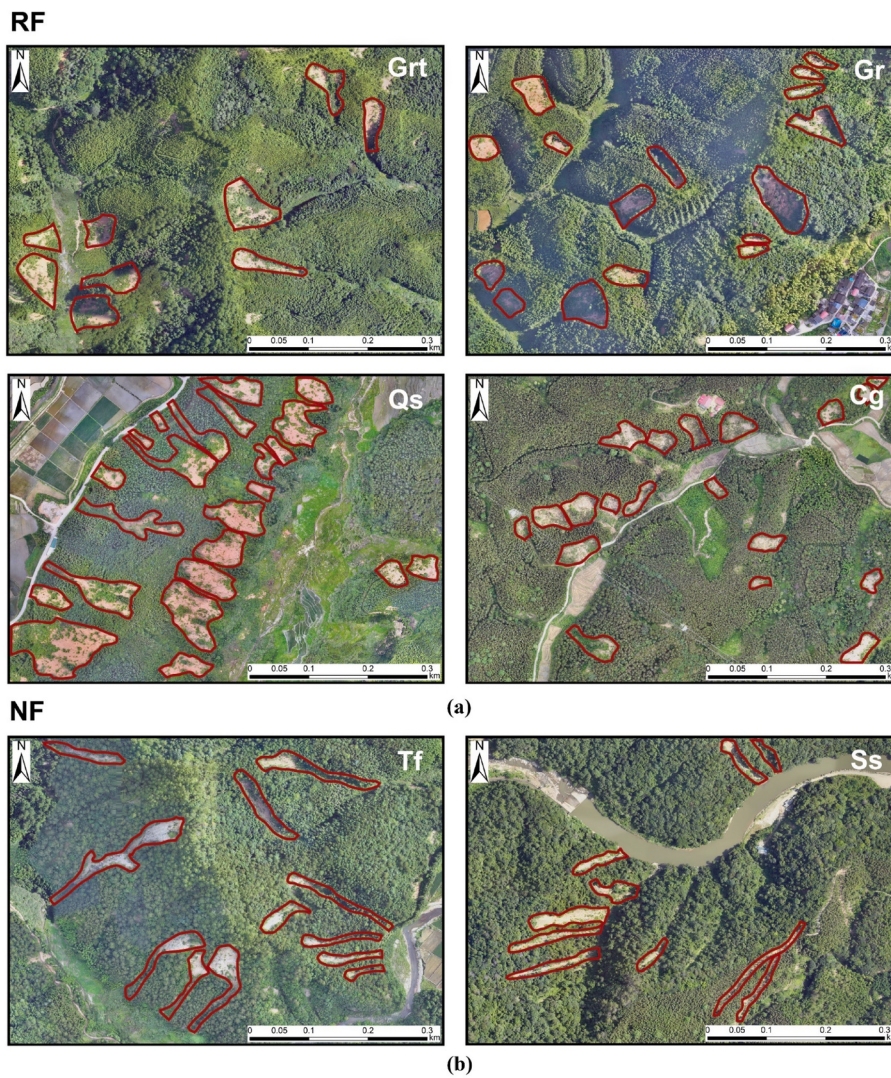


Fig. 9. Two distinct landslide patterns in (a) RF ecosystems (Grt, Gr, Cg, and Qs zones) and (b) NF ecosystems (Tf and Ss zones).

on south-facing slopes with higher slope gradient, larger relative elevation differences, larger area and higher L/W, shown in Fig. 8a. These landslides are characterized by consistently negative plane and profile curvatures, suggesting a preference for convergent and concave landforms. They tend to be elongated and slender (Fig. 8b and 9b), which may serve as precursors to debris flow formation,

particularly when sufficient sediment supply and favorable topographic conditions are available.

5.2. Landslide failure mechanism in RF and NF ecosystems

Stability analysis has been widely applied in landslide early warning

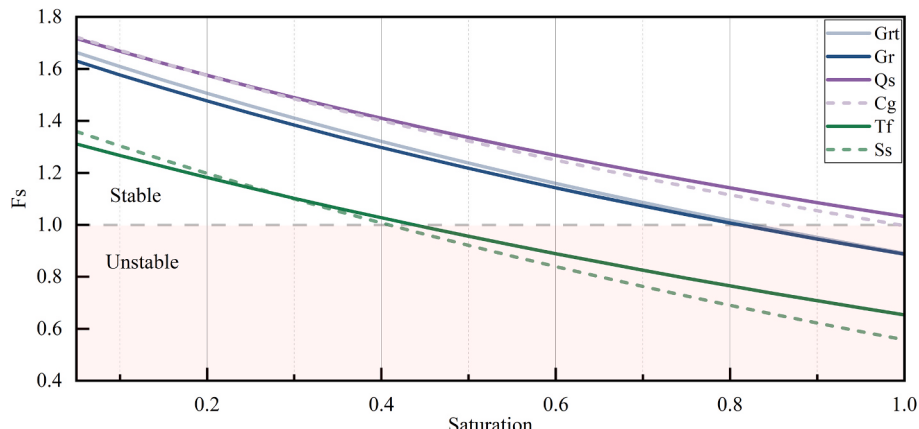


Fig. 10. Variations of slope stability in six lithology zones with changing saturation levels.

and hazard assessment. To gain further insights into the failure mechanisms associated with landslides in NF and RF ecosystems, the stability method accounting for the mechanical effects of vegetation as introduced in section 3.3, is employed herein to evaluate slope stability under varying saturation conditions across six lithological zones. All the values of parameters employed in equation (4) for the stability calculations are provided in Table S2. As presented in Fig. 10, the results indicate that, under identical infiltration conditions, slopes within Tf and Ss zones of the NF ecosystems exhibit lower stability and are more susceptible to landslides compared to those in lithological zones within RF ecosystems. This observation suggests alternative triggering mechanisms that may differ from those reported in previous studies (Baum et al., 2010; Matsushi et al., 2006; McGuire et al., 2016; Montgomery et al., 2009). In the NF ecosystems, where *Pinus massoniana* is the dominant tree species, both the root area ratio (RAR) and root density are significantly lower across soil layers compared to those of *Cunninghamia lanceolata* (Lamb.) Hook. in RF ecosystems (Table 1). The average tensile strength of roots also presents the similar tendency. These differences collectively lead to a reduced soil-root cohesion, ultimately contributing to the decreased slope stability observed in the NF ecosystems.

However, as revealed in section 4.1, both the landslide quantity and density in RF ecosystems are higher than those in NF ecosystems. More lithology zones are employed for large-scale cultivation of commercial tree species, which can explain the larger number of landslide quantity in RF ecosystems. The observed variations in landslide density between NF and RF ecosystems may be attributed to the differences of slope hydrological process under the effect of lithology-vegetation interaction, which highlights the contrasting landslide initiation mechanisms.

In RF ecosystems, the dense plantation of artificial forests (*Cunninghamia lanceolata* (Lamb.) Hook.) and their shallow roots promote the formation of intensive preferential flow networks within the slope. These networks can transmit up to 74–100 % of infiltrating water (Alaoui & Helbling, 2006), reorganizing hillslope infiltration and moisture redistribution, drive percolation below the root zone toward potential slip surfaces, and thus significantly affect the slope stability (Deng et al., 2025; Greco et al., 2023; Vergani et al., 2017; Yu et al., 2025). Field observations confirm that landslides in RF ecosystems typically develop within deeper residual soil layers, as illustrated in Fig. 11a.

In NF ecosystem, the hydrological process affected by both the

vegetation condition and the lithological discontinuities determine the slope stability. Due to minimal human disturbance, the structurally diverse canopy and surface biological soil crusts in NF ecosystems can enhance rainfall interception, thereby reducing effective infiltration on hillslopes (Levia & Germer, 2015). This interception effect likely delays or suppresses the downward migration of rainwater toward potential slip surfaces, thereby influencing slope hydrological response and potentially decreasing the likelihood of slope failure. Moreover, in NF lithological zones, a thin residual mantle overlaying the weathered bedrock were observed in the soil profiles of the studied sites. This leads to the permeability contrast between these layers, promoting the perched water and elevated pore pressures above the soil-bedrock interface during heavy rainfall. It causes the reduce of the effective stress and shear strength, facilitating the formation of a sliding surface, ultimately triggering shallow landslide initiation (Fig. 11b). Overall, the lithological zones are characterized by lower vegetation density and less developed subsurface root networks, which indicating the limited control of vegetation on subsurface hydrological processes and mechanical reinforcement.

Therefore, while the homogeneity of densely planted tree species in RF ecosystems contributes to enhanced slope stability through mechanical reinforcement (i.e., higher factor of safety), the combination of aboveground and belowground vegetation characteristics in densely planted forests, particularly the shallow root systems that promote the formation of intensive preferential flow networks, also facilitates rainfall infiltration toward the potential sliding surface. This hydrological mechanism accounts for the paradoxical observation of high landslide density in RF ecosystems despite the enhanced slope stability by root mechanical contribution (Xu et al., 2024). These findings highlight the potential benefit of incorporating deep-rooted species into forest restoration strategies to disrupt preferential flow pathways and the importance of appropriately regulating planting density to mitigate the amplifying effect of stemflow on rainfall redistribution, which thereby reduces the possibility of landslide initiation and the magnitude of failures in RF ecosystems (Di Prima et al., 2023; Pinos et al., 2023; Kunadi et al., 2024; Levia & Germer, 2015). In contrast, the NF ecosystems is characterized by a shallow soil layer overlying bedrock, which constrains the development and effectiveness of deep-rooted vegetation-based slope stabilization measures. The strategies considering diverse canopy structure to enhance rainfall interception and

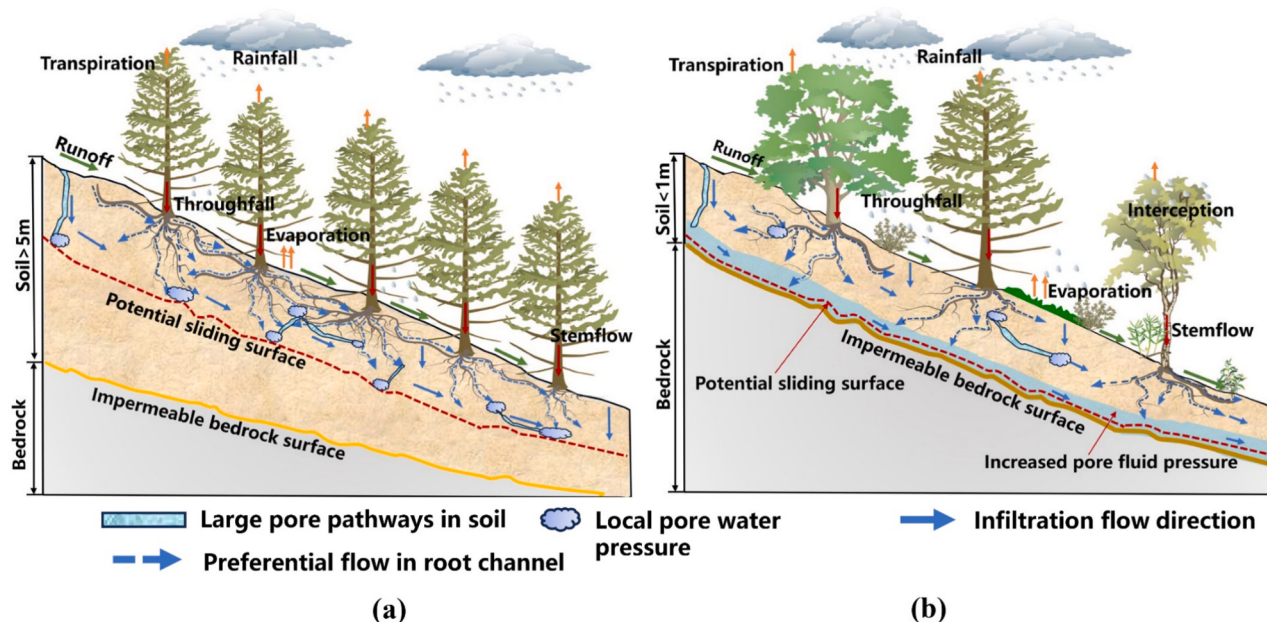


Fig. 11. Illustrative diagrams of (a) landslides in RF developed within residual soil layers, and (b) landslides in NF developed on the soil-bedrock interface.

reduce subsurface water accumulation may be a superior choice in landslide prevention for NF ecosystems. Consequently, the development of ecosystem-specific ecological management strategies is suggested to adapt to the distinct lithological and vegetative conditions of RF and NF ecosystems, which is critical for improving the effectiveness of landslide mitigation efforts while supporting sustainable ecological and economic development.

5.3. Study limitations and outlook

This study investigates the distinct failure patterns and mechanisms associated with different lithology-vegetation systems. However, several limitations should be noted. First, the hydrological effects of different forest types were not directly compared under uniform lithological conditions, and the interaction between lithology and vegetation in controlling landslide occurrence remains insufficiently validated. Second, this study applied the Wu model and the limit equilibrium method to evaluate slope stability in restored forest (RF) and native forest (NF) ecosystems. While these approaches provide useful insights into vegetation-related reinforcement and overall stability, they also involve important limitations. As discussed in Section 3, the Wu model is constrained by its simplifying assumptions regarding root distribution and reinforcement mechanisms. It assumes that roots crossing the shear plane act as independent, fully mobilized tensile members, ignoring progressive root breakage, inter-root interactions, and the nonlinear stress-strain behavior of root-soil systems. The model also neglects the spatial heterogeneity of root architecture and temporal changes in root properties caused by growth, decay, or variations in soil moisture. Consequently, the Wu model often provides an upper-bound estimate of root cohesion rather than a realistic representation of root reinforcement in natural slopes. These limitations underscore the need to develop process-based models that better integrate root biomechanics, soil-root interactions, and hydrological dynamics when assessing vegetation effects on slope stability. Similarly, the limit equilibrium method, while widely used, neglects slope deformation and strain compatibility and fails to represent the transient and dynamic response of slopes under varying hydrological conditions. These limitations highlight the need for more advanced approaches that can explicitly incorporate soil-atmosphere-plant interactions and capture the temporal variability of slope stability (An et al., 2018). Such advances will be critical for improving predictive accuracy and for providing robust theoretical support to early warning systems and prevention strategies for shallow landslides in forested landscapes.

6. Conclusions

A comprehensive investigation based on remote sensing interpretation, field investigations, laboratory and in-situ experiments, as well as numerical simulations, are conducted in a representative group-occurring landslide event in southeastern China. The spatial distribution and geometric characteristics of landslides are analyzed. Their geomorphology condition, lithology condition, above- and below-ground vegetation characteristics are studied in depth, elucidating the distinct landslide patterns and failure mechanisms in RF and NF ecosystems. The main conclusions are summarized as follows:

- In terms of the spatial distribution, both the landslide quantity and density in RF ecosystems are higher than those in NF ecosystems. The observed landslides are mainly small and medium sizes with areas in the value range of 200–3000 m². Two distinct landslide patterns can be identified within RF and NF ecosystems: pattern 1 in RF ecosystems with the morphological features predominantly as short and wide, typically inducing localized and rapid surface disruptions with limited potential for triggering secondary hazards. In contrast, pattern 2 in NF ecosystems tend to be elongated and slender, which may serve as precursors to debris flow formation, particularly when

sufficient sediment supply and favorable topographic conditions are available.

- Field investigations of geomorphology, lithology and vegetation conditions indicate that vegetation characteristics are strongly influenced by slope topography, geomorphic attributes, and soil properties, which collectively drive different land-use patterns (NF and RF ecosystems) across the six lithological zones. The combined effect of them leads to the different slope failure mechanisms: the landslides typically develop within deeper residual soil layers in RF ecosystems, while those in NF ecosystems are primarily controlled by lithological discontinuities at the soil-bedrock interface.
- Under identical infiltration conditions, slopes within the NF ecosystems exhibit lower stability and are more susceptible to landslides compared to those in lithological zones within the RF ecosystems. This observation differs from those reported in previous studies, suggesting the necessary to consider both the mechanical and hydrological process governed by different forest management measures on the slope stability. The homogeneity of densely planted tree species in the RF ecosystems contributes to enhanced slope stability through mechanical reinforcement. However, the hydrological mechanism, e.g., the shallow root systems that promote the formation of intensive preferential flow networks, also facilitates rainfall infiltration toward the potential sliding surface, which may account for the paradoxical observation of higher landslide density in the RF ecosystems compared to that in the NF ecosystems.
- The results reveal distinct failure mechanisms across the studied lithology-vegetation systems, however they are limited by simplified stability models and insufficient consideration of lithology-vegetation interactions. Future research should combine field observations, remote sensing, and process-based modeling to better capture soil-atmosphere-plant interactions and improve landslide prediction in forested regions. Moreover, this work also highlights the development of ecosystem-specific ecological management strategies adapted to the distinct lithology-vegetation systems of RF and NF ecosystems, which is critical for improving the effectiveness of landslide mitigation efforts while supporting sustainable ecological and economic development. For instance, incorporating deep-rooted species into forest restoration strategies may provide superior performance in mitigating the landslide initiation in RF ecosystems than NF ecosystems due to the thicker soil layer overlying bedrock.

7. Data availability statement

Statistical values of landslide characteristics in six lithology zones, all the values of parameters employed in equation (4) for slope stability calculations, field survey site information and DEM data of the studied site are available in Zenodo repositories via <https://zenodo.org/records/17153185>

CRediT authorship contribution statement

Ni An: Writing – review & editing, Writing – original draft, Supervision, Project administration, Investigation, Conceptualization. **Zhisheng Dai:** Writing – original draft, Validation, Software, Investigation, Data curation. **Xie Hu:** Writing – review & editing, Software, Resources, Conceptualization. **Buqing Wang:** Validation, Resources, Investigation. **Zhitao Huo:** Resources, Methodology, Investigation. **Yuxin Xiao:** Resources, Methodology, Investigation. **Wei Zhan:** Writing – review & editing, Investigation, Formal analysis. **Yongyong Yang:** Validation, Methodology, Investigation.

Declaration of competing interest

The authors declare that they have no known competing financial interests or personal relationships that could have appeared to influence

the work reported in this paper.

Acknowledgements

The authors wish to acknowledge the financial support of the National Natural Science Foundation of China (42207171), National Key R&D Program of China (2024YFC3012605), Open Foundation of the Key Laboratory of Coupling Process and Effect of Natural Resources Elements (2024KFKT008), Fundamental Research Funds for the Zhejiang Provincial Universities (226-2024-00193) and China Geological Survey – Observation, Monitoring, and Evaluation of Natural Resources and Surface Substrates in the Jiangnan Hilly Region (DD20230515). The authors would like to thank Mr. Yanpeng Fan in Nanping Municipal Bureau of Natural Resources, Mr. Jijun Ren, Mr. Zhihao Zhao and other staffs from the Changsha Natural Resources Comprehensive Investigation Center, China Geological Survey, for their support in the field investigation work.

Appendix A. Supplementary data

Supplementary data to this article can be found online at <https://doi.org/10.1016/j.catena.2025.109452>.

References

- Alaoui, A., Helbling, A., 2006. Evaluation of soil compaction using hydrodynamic water content variation: Comparison between compacted and non-compacted soil. *Geoderma* 134 (1–2), 97–108. <https://doi.org/10.1016/j.geoderma.2005.08.016>.
- An, N., Tang, C.S., Xu, S.K., Gong, X.P., Shi, B., Inyang, H.I., 2018. Effects of soil characteristics on moisture evaporation. *Engineering geology* 239, 126–135. <https://doi.org/10.1016/j.enggeo.2018.03.028>.
- An, N., Tang, C.S., Cheng, Q., Wang, D.Y., Shi, B., 2020. Application of electrical resistivity method in the characterization of 2D desiccation cracking process of clayey soil. *Engineering Geology* 265, 105416. <https://doi.org/10.1016/j.enggeo.2019.105416>.
- ASTM International, 2023. Standard Test Method for Direct Shear Test of Soils under Consolidated Drained Conditions (ASTM D3080/D3080M-23). ASTM International, West Conshohocken, PA. https://doi.org/10.1520/D3080_D3080M-23.
- Baum, R.L., Godt, J.W., Savage, W.Z., 2010. Estimating the timing and location of shallow rainfall-induced landslides using a model for transient, unsaturated infiltration. *J. Geophys. Res. Earth* 115, F03013. <https://doi.org/10.1029/2009JF001321>.
- Bellugi, D., Milledge, D.G., Dietrich, W.E., McKean, J.A., Perron, J.T., Suderth, E.B., Kazian, B., 2015. A spectral clustering search algorithm for predicting shallow landslide size and location. *J. Geophys. Res. Earth* 120, 300–324. <https://doi.org/10.1002/2014jv003137>.
- Bronson, K.F., Conley, M.M., French, A.N., Hunsaker, D.J., Thorp, K.R., Barnes, E.M., 2020. Which active optical sensor vegetation index is best for nitrogen assessment in irrigated cotton? *Agron. J.* 112, 2205–2218. <https://doi.org/10.1002/agj2.20120>.
- China News Service Online, 2024. Heavy rainstorm in Zixing, Hunan Province kills 50 people and leaves 15 missing, CCTV News, available at <https://www.china-news-online.com/h5/lang/Canada/66299.html> (accessed 4 Mar. 2025).
- Dai, F.C., Lee, C.F., Ngai, Y.Y., 2002. Landslide risk assessment and management: an overview. *Engineering Geology* 64, 65–87. [https://doi.org/10.1016/s0013-7952\(01\)00093-x](https://doi.org/10.1016/s0013-7952(01)00093-x).
- Dai, Z., Ma, C., Miao, L., Li, M., Wu, J., Wang, X., 2022. Initiation conditions of shallow landslides in two man-made forests and back estimation of the possible rainfall threshold. *Landslides* 19 (5), 1031–1044. <https://doi.org/10.1007/s10346-021-01823-1>.
- De Jesús Arce-Mojica, T., Nehren, U., Sudmeier-Rieux, K., Miranda, P.J., Anhuf, D., 2019. Nature-based solutions (NbS) for reducing the risk of shallow landslides: where do we stand? *Int. J. Disaster Risk Reduct.* 41, 101293. <https://doi.org/10.1016/j.ijdr.2019.101293>.
- Deng, J., Ma, C., Zhang, Y., 2022. Shallow landslide characteristics and its response to vegetation by example of July 2013 extreme rainstorm, Central Loess Plateau, China. *Bulletin of Engineering Geology and the Environment* 81 (3), 100. <https://doi.org/10.1007/s10064-022-02606-1>.
- Deng, Z., Lan, H., Li, L., Sun, W., 2025. Vegetation-induced modifications in hydrological processes and the consequential dynamic effects of slope stability. *Catena* 251, 108793. <https://doi.org/10.1016/j.catena.2025.108793>.
- Depicker, A., Jacobs, L., Mboga, N., Smets, B., Rompaey, A.V., Lennert, M., Wolff, E., Kervyn, F., Michellier, C., Dewitte, O., Govers, G., 2021. Historical dynamics of landslide risk from population and forest-cover changes in the Kivu Rift. *Nature Sustainability* 4, 965–974. <https://doi.org/10.1038/s41893-021-00757-9>.
- Di Prima, S., Fernandes, G., Marras, E., Giadrossich, F., Stewart, R.D., Abou Najm, M.R., Winiarski, T., Mourier, B., Angulo-Jaramillo, R., Comegna, A., Del Campo, A., Lassabatere, L., 2023. Evaluating subsurface flow connectivity in a pine-covered hillslope with stemflow infiltration and ground-penetrating radar surveys. *Journal of Hydrology* 620, 129527. <https://doi.org/10.1016/j.jhydrol.2023.129527>.
- Egas, H.M., Stabile, R.A., De Andrade, M.R.M., Michel, G.P., De Araújo, J.P.C., Michel, R. D.L., Gonçalves, S.T., Nery, T.D., De Paula, D.S., Reckziegel, E.W., 2024. Comprehensive inventory and initial assessment of landslides triggered by autumn 2024 rainfall in Rio Grande do Sul, Brazil. *Landslides* 22, 579–589. <https://doi.org/10.1007/s10346-024-02410-w>.
- Forte, G., Pirone, M., Santo, A., Nicotera, M.V., Urciuoli, G., 2019. Triggering and predisposing factors for flow-like landslides in pyroclastic soils: the case study of the Lattari Mts. (southern Italy). *Eng. Geol.* 257, 105–137. <https://doi.org/10.1016/j.enggeo.2019.05.014>.
- Fu, Y., 2023. Geohazards susceptibility and regional disaster resilience assessment in the southeastern hilly region. Master's Thesis, Hunan University, Changsha, China. <https://doi.org/10.27135/d.cnki.ghudu.2023.000762>. (In Chinese).
- Giarola, A., Schoorl, J.M., Baartman, J.E.M., Bordon, M., Tarolli, P., Zucca, F., Heckmann, T., Meisina, C., 2024. Exploiting the land use to predict shallow landslide susceptibility: probabilistic implementation of LAPUS-LS. *Catena* 246, 108437. <https://doi.org/10.1016/j.catena.2024.108437>.
- Greco, R., Marino, P., Bogaard, T.A., 2023. Recent advancements of landslide hydrology. *Wiley Interdisciplinary Reviews: Water* 10 (6), e1675. <https://doi.org/10.1002/wat2.1675>.
- Guo, Y., Ma, C., 2023. Elucidating the role of soil hydraulic properties on aspect-dependent landslide initiation. *Hydrology and Earth System Sciences* 27 (8), 1667–1682. <https://doi.org/10.5194/hess-27-1667-2023>.
- Haque, U., da Silva, P.F., Devoli, G., Pilz, J., Zhao, B., Khaloua, A., Wilopo, W., Andersen, P., Lu, P., Lee, J., Yamamoto, T., Keelings, D., Wu, J.-H., Glass, G.E., 2019. The human cost of global warming: Deadly landslides and their triggers (1995–2014). *Science of the Total Environment* 682, 673–684. <https://doi.org/10.1016/j.scitotenv.2019.03.415>.
- Hartmann, A., Blume, T., 2024. The evolution of hillslope hydrology: links between form, function and the underlying control of geology. *Water Resources Research* 60, e2023WR035937. <https://doi.org/10.1029/2023WR035937>.
- Hu, C., Zhang, X., 2020. Loess Plateau soil erosion governance and runoff-sediment variation of Yellow River. *Water Resour. Hydropower Eng.* 51, 1–11. <https://doi.org/10.13928/j.cnki.wrahe.2020.01.001>. (In Chinese).
- Huang, S., Tang, L., Hupy, J.P., Wang, Y., Shao, G., 2020. A commentary review on the use of normalized difference vegetation index (NDVI) in the era of popular remote sensing. *Journal of Forestry Research* 32, 1–6. <https://doi.org/10.1007/s11676-020-01155-1>.
- IAEG Commission on Landslides, 1990. Suggested nomenclature for landslides. *Bulletin of the International Association of Engineering Geology* 41, 13–16. <https://doi.org/10.1007/BF02590202>.
- IPCC, 2006. 2006 IPCC Guidelines for National Greenhouse Gas Inventories. Volume 4: Agriculture, Forestry and Other Land Use. Institute for Global Environmental Strategies (IGES), Hayama, Japan. Available at: <https://www.ipcc-nggip.iges.or.jp/public/2006gl/vol4.html> (accessed 17 August 2025).
- IPCC, 2022. Climate Change 2022: Impacts, Adaptation, and Vulnerability, edited by H.-O. Pörtner et al. Cambridge Univ. Press, Cambridge, U.K., and New York, N.Y., 1017/9781009325844.
- IUSS Working Group WRB, 2022. World Reference Base for Soil Resources: International soil classification system for naming soils and creating legends for soil maps. 4th ed. International Union of Soil Sciences (IUSS), Vienna. Available at: <https://www.isric.org/explore/wrb> (accessed 17 August 2025).
- Kim, J.H., Fourcaud, T., Jourdan, C., Maeght, J.-L., Mao, Z., Metayer, J., Meylan, L., Pierret, A., Rapidel, B., Roupsard, O., de Rouw, A., Sanchez, M.V., Wang, Y., Stokes, A., 2017. Vegetation as a driver of temporal variations in slope stability: the impact of hydrological processes. *Geophysical Research Letters* 44 (10), 4897–4907. <https://doi.org/10.1002/2017gl073174>.
- Kunadi, A.S., Lardner, T., Silberstein, R.P., Leopold, M., Callow, N., Veneklaas, E., Puri, A., Sydney, E., Thompson, S.E., 2024. Introducing pour points: characteristics and hydrological significance of a rainfall-concentrating mechanism in a water-limited woodland ecosystem. *Water Resources Research* 60, e2023WR035458. <https://doi.org/10.1029/2023wr035458>.
- Leshchinsky, B., Olsen, M.J., Mohney, C., O'Banion, M., Bunn, M., Allan, J., McClung, R., 2019. Quantifying the sensitivity of progressive landslide movements to failure geometry, undercutting processes and hydrological changes. *Journal of Geophysical Research: Earth Surface* 124 (2), 616–638. <https://doi.org/10.1029/2018JF004833>.
- Levia, D.F., Germer, S., 2015. A review of stemflow generation dynamics and stemflow-environment interactions in forests and shrublands. *Reviews of Geophysics* 53 (3), 673–714. <https://doi.org/10.1002/2015RG000479>.
- Li, B.V., Jenkins, C.N., Xu, W., 2022. Strategic protection of landslide vulnerable mountains for biodiversity conservation under land-cover and climate change impacts. *Proceedings of the National Academy of Sciences* 119, e2113416118. <https://doi.org/10.1073/pnas.2113416118>.
- Liu, D., 1997. Segmentation of the Shaowu-Heyuan fault zone and their activity assessment. *Journal of Geomechanics*, 3(2), 7. <https://doi.org/10.1007/s10038-007-0007-0>. (In Chinese).
- Maraun, D., Knevels, R., Mishra, A.N., Truhetz, H., Bevacqua, E., Proske, H., Zappa, G., Brenning, A., Petschko, H., Schaffer, A., Leopold, P., Puxley, B.L., 2022. A severe landslide event in the Alpine foreland under possible future climate and land-use changes. *Communications Earth & Environment* 3, 1–11. <https://doi.org/10.1038/s43247-022-00408-7>.
- Matsushita, Y., Hattanji, T., Matsukura, Y., 2006. Mechanisms of shallow landslides on soil-mantled hillslopes with permeable and impermeable bedrocks in the Boso Peninsula, Japan. *Geomorphology* 76 (1–2), 92–108. <https://doi.org/10.1016/j.geomorph.2005.10.003>.

- McColl, S.T., Cook, S.J., 2024. A universal size classification system for landslides. *Landslides* 21 (1), 111–120. <https://doi.org/10.1007/s10346-023-02131-6>.
- McGuire, L.A., Rengers, F.K., Kean, J.W., Coe, J.A., Mirus, B.B., Baum, R.L., Godt, J.W., 2016. Elucidating the role of vegetation in the initiation of rainfall-induced shallow landslides: Insights from an extreme rainfall event in the Colorado Front Range. *Geophysical Research Letters* 43 (17), 9084–9092. <https://doi.org/10.1002/2016gl070741>.
- Milledge, D.G., Bellugi, D., McKean, J.A., Densmore, A.L., Dietrich, W.E., 2014. A multidimensional stability model for predicting shallow landslide size and shape across landscapes. *Journal of Geophysical Research: Earth Surface* 119 (11), 2481–2504. <https://doi.org/10.1002/2014jf003135>.
- Montgomery, D.R., Dietrich, W.E., 1994. A physically based model for the topographic control on shallow landsliding. *Water Resources Research* 30 (4), 1153–1171. <https://doi.org/10.1029/93WR02979>.
- Montgomery, D.R., Schmidt, K.M., Dietrich, W.E., McKean, J., 2009. Instrumental record of debris flow initiation during natural rainfall: implications for modeling slope stability. *Journal of Geophysical Research: Earth Surface* 114 (F1), 2008JF001078. <https://doi.org/10.1029/2008JF001078>.
- Ohlmacher, G.C., 2007. Plan curvature and landslide probability in regions dominated by Earth flows and Earth slides. *Engineering Geology* 91 (2–4), 117–134. <https://doi.org/10.1016/j.enggeo.2007.01.005>.
- Ozturk, U., Bozzolan, E., Holcombe, E.A., Shukla, R., Pianosi, F., Wagener, T., 2022. How climate change and unplanned urban sprawl bring more landslides. *Nature* 608 (7922), 262–265. <https://doi.org/10.1038/d41586-022-02141-9>.
- Paronuzzi, P., Bolla, A., 2023. Rainfall infiltration and slope stability of alpine colluvial terraces subject to storms (NE Italy). *Engineering Geology* 323, 107199. <https://doi.org/10.1016/j.enggeo.2023.107199>.
- Phillips, C., Betts, H., Smith, H.G., Tsypolenkov, A., 2024. Exploring the post-harvest ‘window of vulnerability’ to landslides in New Zealand steepland plantation forests. *Ecological Engineering* 206, 107300. <https://doi.org/10.1016/j.ecoleng.2024.107300>.
- Pinos, J., Flury, M., Latron, J., Llorens, P., 2023. Routing stemflow water through the soil via preferential flow: a dual-labelling approach with artificial tracers. *Hydrology and Earth System Sciences* 27 (15), 2865–2881. <https://doi.org/10.5194/hess-27-2865-2023>.
- Pohl, M., Alig, D., Körner, C., Rixen, C., 2009. Higher plant diversity enhances soil stability in disturbed alpine ecosystems. *Plant and Soil* 324 (1–2), 91–102. <https://doi.org/10.1007/s11104-009-9906-3>.
- Preti, F., 2006. Stabilità dei versanti vegetati, in *Manuale di ingegneria naturalistica*, vol. 3, edited by G. Sauli, P. Cornellini, and F. Preti, pp. 137–168. <https://www.researchgate.net/publication/266876677>.
- Qiu, H., Su, L., Tang, B., Yang, D., Ullah, M., Zhu, Y., Kamp, U., 2024. The effect of location and geometric properties of landslides caused by rainstorms and earthquakes. *Earth Surface Processes and Landforms* 49 (7), 2067–2079. <https://doi.org/10.1002/esp.5816>.
- Rana, K., Ozturk, U., Malik, N., 2021. Landslide geometry reveals its trigger. *Geophysical Research Letters* 48 (4), e2020GL090848. <https://doi.org/10.1029/2020GL090848>.
- Sakals, M.E., Sidle, R.C., 2004. A spatial and temporal model of root cohesion in forest soils. *Canadian Journal of Forest Research* 34 (4), 950–958. <https://doi.org/10.1139/x03-268>.
- Sassa, K., 2013. International Programme on Landslides. In: Sassa, K., Rouhbani, B., Briceño, S., McSaveney, M., He, B. (Eds.), *Landslides: Global Risk Preparedness*. Springer, Berlin, Heidelberg, pp. 3–24. https://doi.org/10.1007/978-3-642-22087-6_1.
- Sato, T., Shuin, Y., 2025. Variation in the frequency and characteristics of landslides in response to changes in forest cover and rainfall in Japan over the last century: a literature review. *Catena* 249, 108639. <https://doi.org/10.1016/j.catena.2024.108639>.
- Schmidt, K.M., Roering, J.J., Stock, J.D., Dietrich, W.E., Montgomery, D.R., Schaub, T., 2001. The variability of root cohesion as an influence on shallow landslide susceptibility in the Oregon coast range. *Canadian Geotechnical Journal* 38 (5), 995–1024. <https://doi.org/10.1139/t01-031>.
- Sheng, B., Wang, H., Li, H., Wu, K., Li, Q., 2023. Thermodynamic and dynamic effects of anomalous dragon boat water over South China in 2022. *Weather and Climate Extremes* 40, 100560. <https://doi.org/10.1016/j.wace.2023.100560>.
- Sidle, R.C., Bogaard, T.A., 2016. Dynamic earth system and ecological controls of rainfall-initiated landslides. *Earth-Science Reviews* 159, 275–291. <https://doi.org/10.1016/j.earscirev.2016.05.013>.
- Staley, S.E., Fawcett, P.J., Jiménez-Moreno, G., Anderson, R.S., Markgraf, V., Brown, E. T., 2023. Long-term landscape evolution in response to climate change, ecosystem dynamics, and fire in a basaltic catchment on the Colorado Plateau. *Journal of Geophysical Research: Earth Surface* 128 (12), e2023JF007266. <https://doi.org/10.1029/2023JF007266>.
- Stokes, A., Atger, C., Bengough, A.G., Fourcaud, T., Sidle, R.C., 2009. Desirable plant root traits for protecting natural and engineered slopes against landslides. *Plant and Soil* 324 (1–2), 1–30. <https://doi.org/10.1007/s11104-009-0159-y>.
- Taylor, F.E., Malamud, B.D., Witt, A., Guzzetti, F., 2018. Landslide shape, ellipticity and length-to-width ratios. *Earth Surface Processes and Landforms* 43 (15), 3164–3189. <https://doi.org/10.1002/esp.4479>.
- Tian, Y., Xu, C., Chen, J., Zhou, Q., Shen, L., 2017. Geometrical characteristics of earthquake-induced landslides and correlations with control factors: a case study of the 2013 Minxian, Gansu, China, Mw 5.9 event. *Landslides* 14 (6), 1915–1927. <https://doi.org/10.1007/s10346-017-0835-6>.
- Vergani, C., Giadrossich, F., Buckley, P., Conedera, M., Pividori, M., Salbitano, F., Rauch, H.S., Lovreglio, R., Schwarz, M., 2017. Root reinforcement dynamics of European coppice woodlands and their effect on shallow landslides: a review. *Earth-Science Reviews* 167, 88–102. <https://doi.org/10.1016/j.earscirev.2017.02.002>.
- Wang, F., Wang, G., Cui, J., Guo, L., Mello, C.R., Boyer, E.W., Tang, X., Yang, Y., 2022. Preferential flow patterns in forested hillslopes of east Tibetan Plateau revealed by dye tracing and soil moisture network. *European Journal of Soil Science* 73 (4), e13294. <https://doi.org/10.1111/ejss.13294>.
- Wood, J.L., Harrison, S., Turkington, T.A.R., Reinhardt, L., 2016. Landslides and synoptic weather trends in the European Alps. *Climatic Change* 136 (2), 297–308. <https://doi.org/10.1007/s10584-016-1623-3>.
- Wu, T.H., McKinnell III, W.P., Swanston, D.N., 1979. Strength of tree roots and landslides on Prince of Wales Island, Alaska. *Canadian Geotechnical Journal* 16 (1), 19–33. <https://doi.org/10.1139/179-003>.
- Xu, Y., Luo, L., Guo, W., Jin, Z., Tian, P., Wang, W., 2024. Revegetation Changes Main Erosion Type on the Gully-Slope on the Chinese Loess Plateau Under Extreme Rainfall: Reducing Gully Erosion and Promoting Shallow Landslides. *Water resources research* 60 (3). <https://doi.org/10.1029/2023wr036307>.
- Yu, Y., Hua, T., Chen, L., Zhang, Z., Pereira, P., 2024. Divergent changes in vegetation greenness, productivity, and rainfall use efficiency are characteristic of ecological restoration towards high-quality development in the Yellow River basin, China. *Engineering* 34, 109–119. <https://doi.org/10.1016/j.eng.2023.07.012>.
- Yu, Y., Xu, Z., Yang, Y., An, N., 2025. Numerical investigation into the formation of pipe flow and the influencing factors in soil-rock mixtures. *Computers and Geotechnics* 185, 107342. <https://doi.org/10.1016/j.compgeo.2025.107342>.
- Zhuang, J., Peng, J., Du, C., Zhu, Y., Kong, J., 2024. Shallow-landslide stability evaluation in loess areas according to the Revised Infinite Slope Model: a case study of the 7.25 Tianshui sliding-flow landslide events of 2013 in the southwest of the Loess Plateau, China. *Natural hazards and earth system sciences* 24 (7), 2615–2631. <https://doi.org/10.5194/nhess-24-2615-2024>.